The impact of cloudiness and cloud type on the atmospheric heating rate of black and brown carbon

Luca Ferrero[1,*], Asta Gregorič[2,3], Grisa Močnik[3,4], Martin Rigler[2], Sergio Cogliati[1,5], Francesca

Barnaba[6], Luca Di Liberto[6], Gian Paolo Gobbi[6], Niccolò Losi[1] and Ezio Bolzacchini[1]

[1]GEMMA and POLARIS Research Centers, Department of Earth and Environmental Sciences, University of Milano-Bicocca, Piazza della Scienza 1, 20126, Milan, Italy.

[2]Aerosol d.o.o., Kamniška 39A, SI-1000 Ljubljana, Slovenia.

[3]Center for Atmospheric Research, University of Nova Gorica, Vipavska 11c, SI-5270 Ajdovščina, Slovenia.

[4]Department of Condensed Matter Physics, Jozef Stefan Institute, SI-1000 Ljubljana, Slovenia.

[5]Remote Sensing of Environmental Dynamics Lab., DISAT, University of Milano-Bicocca, P.zza della Scienza 1, 20126, Milano, Italy

[6]ISAC -CNR, Roma - Tor Vergata, Via Fosso Del Cavaliere 100, 00133, Roma, Italy.

Correspondence to: Luca Ferrero (luca.ferrero@unimib.it)

Abstract. We experimentally quantified the impact of cloud fraction and cloud type on the heating rates (HRs) of black and brown carbon (HR_{BC} and HR_{BrC}).In particular, in this work, we examine in more detail the average cloud effect (Ferrero et al., 2018) using high time-resolution measurements of aerosol absorption at multiple-wavelengths coupled with spectral measurements of the direct, diffuse and surface reflected radiation and lidar data in the Po Valley. The experimental set-up allowed a direct determination of HR_{BC} and HR_{BrC} in any sky condition. The highest values of total HR were found in the middle of the winter (1.43 ± 0.05 K day^{-1}) while the lowest in spring (0.54 ± 0.02 K day^{-1}) Overall the HR_{BrC} accounted for $13.7\pm0.2\%$ of the total HR, the BrC being characterized by an AAE of 3.49 ± 0.01.

Simultaneously, sky conditions were classified (from clear-sky to cloudy) in terms of fraction of sky covered by clouds (oktas) and cloud types. Cloud types were grouped as a function of altitude into the following classes: 1) low level (<2 km) stratus, cumulus and stratocumulus; 2) middle level (2-7 km) altostratus, altocumulus; 3) high level (> 7 km) cirrus, cirrocumulus-cirrostratus. Measurements carried out in different sky conditions at high-time resolution showed a constant decrease of HR with increasing cloudiness of the atmosphere enabling us to quantify for the first time the bias (in %) in the aerosol HR introduced by improperly assuming clear-sky conditions in radiative transfer calculations. In fact, during the campaign, clear sky conditions were only present 23% of the time while the remaining time (77%) was characterized by cloudy conditions. Our results show that, by incorrectly assuming clear-sky conditions, the HR of light absorbing aerosol can be largely overestimated (by 50% in low cloudiness, oktas=1-2), up to over 400% (in complete overcast conditions, i.e., oktas=7-8). The impact of different cloud types on the HR compared to a clear sky condition was also investigated. Cirrus were found to have a modest impact, decreasing the HR_{BC} and HR_{BrC} by -1 – -5%. Cumulus decreased the HR_{BC} and HR_{BrC} by -31 ± 12 and $-26\pm7\%$, respectively, while cirrocumulus-cirrostratus by -60 ± 8 and $-54\pm4\%$, which was comparable to the impact

of altocumulus (-60±6 and -46±4%). A high impact on HR_{BC} and HR_{BrC} was found for stratocumulus (-63±6 and -58±4%, respectively) and altostratus (-78±5 and -73±4%, respectively), although the highest impact was found to be associated to stratus that suppressed the HR_{BC} and HR_{BrC} by -85±5 and -83±3%, respectively. Additionally, the cloud influence on the radiation spectrum that interacts with the absorbing aerosol was investigated. Black and brown carbon (BC and BrC) have different spectral responses (a different absorption Angstrom exponent, AAE) and our results show that the presence of clouds causes a greater decrease for the HR_{BC} with respect to to HR_{BrC} going clear sky to complete overcast conditions; the observed the difference is 12±6%. This means that, compared to BC, BrC is more efficient in heating the surrounding atmosphere in cloudy conditions than in clear sky. Overall, this study extends the results of a previous work (Ferrero et al., 2018), highlighting the need to take into account both the role of cloudiness and of different cloud types to better estimate the HR associated to both BC and BrC, and in turn decrease the uncertainties associated to the quantification of the impact of these species on radiation and climate.

1   Introduction

The impact of aerosols on climate is traditionally investigated focusing on their direct, indirect and semi-direct effects (Bond et al., 2013; IPCC, 2013; Ferrero et al., 2018, 2014; Bond et al., 2013; Ramanathan and Feng, 2009; Koren et al. 2008; Koren et al., 2004;Kaufman et al., 2002). Direct effects are related to the sunlight interaction with aerosols trough absorption and scattering, indirect effects are related to the ability of aerosol to act as cloud condensation nuclei affecting the clouds' formation and properties, semi-direct effects are those related to a feedback on cloud evolution affecting other atmospheric parameters (e.g. the thermal structure of the atmosphere) (Ramanathan and Feng, 2009; Koren et al. 2008; IPCC, 2013; Koren et al., 2004; Kaufman et al., 2002).

Both the direct and indirect radiative effects on the climate caused by anthropogenic and natural aerosols still represent major sources of uncertainty (IPCC, 2013); for example the aerosol direct radiative effect (DRE), on a global scale, may switch from positive to negative forcing on short (e.g. daily) time-scales (Lolli et al., 2018; Tosca et al., 2017; Campbell et al., 2016).

This is due to the fact that aerosol is a heterogeneous complex mixture of particles characterized by different size, chemistry, and shape (e.g., Costabile et al., 2013), greatly varying in time and space both in the horizontal and vertical dimension (e.g., Ferrero et al., 2012). On the global scale, most of the values reported for the DRE, used to quantify the aerosol impact on the climate, were derived from models (Bond et al., 2013; Koch and Del Genio, 2010). This has the advantage of providing continuous DRE fields in space and time. However, inaccuracies related to simplified model assumptions on chemistry, shape, and the mixing state of the particles can affect the results (Nordmann et al., 2014; Koch et al., 2009), amplifying the uncertainties on the estimated global and regional aerosol climate effects (Andreae and Ramanathan, 2013). Another important issue is that the aerosol DRE is usually determined in clear-sky conditions/approximations. Although the clear sky approximation is useful when comparing measurements to radiative transfer modelling outcomes during experimental campaigns performed in fair weather conditions (e.g., Ferrero et al., 2014; Ramana et al., 2007), in general this simplification cannot capture the complexity of the phenomenon in the majority of weather conditions (Myhre et al., 2013). In fact, clouds are one of the most important factors modulating the solar radiation that reaches the ground. By scattering and absorbing the radiation passing through them, clouds strongly affect the radiation and also modify the spectrum of

the short-wave radiation, especially in the UV region (Calbó et al., 2005; López et al., 2009). In some specific cases (e.g. cirrus/cumulus clouds), scattering of radiation from the sides of the cloud may enhance global irradiance to the levels higher than those in clear sky conditions (Mims and Frederick, 1994; Feister et al., 2015).

80   Up to now, the role of cloudiness and of cloud type on the aerosol DRE was poorly investigated. Matus et al. (2015) recently used a complex combination of the CLOUDSAT's satellite multi-sensor radiative fluxes and heating rates (HR) products to infer both the DRE at the top-of-atmosphere (TOA) and HR profiles of aerosols that lie above the clouds. The study showed how results were affected by the cloudiness (e.g. cloud fraction) and, for example for the south eastern Atlantic, reported a DRE ranging from -3.1 to -0.6 W m^{-2} going from clear sky

85   to cloudy conditions.

A further investigation by Myhre et al. (2013) reported results of modelling simulations during the AeroCom Project (Phase II): In all sky conditions (thus including the effect of clouds) they estimated an all-sky DRE for total anthropogenic aerosols of -0.27 W m^{-2} (range: −0.58 to −0.02 W m^{-2}), this being about half of the clear sky one. The most important factors responsible for the observed difference were the amount of aerosol absorption,

90   the location of aerosol layers in relation to clouds (above or below), and the cloud distribution. In fact, the presence of absorbing aerosols (i.e. Black Carbon, BC; Brown Carbon, BrC; or mineral dust) might have important effects on the radiative balance. It is estimated that, due to its absorption of sunlight, BC is the second most important positive anthropogenic climate-forcing agent after CO_2 (Bond et al., 2013; Ramanathan and Carmichael, 2008), while BrC contributes ~10-30% to the total absorption on a global scale (Ferrero et al., 2018; Shamjad et al., 2015;

95   Chung et al., 2012; Kumar et al., 2018). As a main difference compared to CO_2, absorbing aerosols are short-lived climate forcers, thus representing a potential global warming mitigation target. However, the real potential benefit of any mitigation strategy should also be based on observational measurements, possibly carried out in all sky conditions.

It also noteworthy that the HR induced by absorbing aerosol can trigger different atmospheric feedbacks. BC and

100 dust can alter the atmospheric thermal structure, thus affecting atmospheric stability, cloud distribution and even synoptic winds such as the monsoons (IPCC, 2013; Bond et al., 2013; Ramanathan and Feng, 2009; Koch et al., 2009; Ramanathan and Carmichael, 2008; Koren et al. 2008; Koren et al., 2004; Kaufman et al., 2002). Even in this case, the feedbacks should be quantified on the basis of HR measurements carried out in any sky conditions. In agreement with the aforementioned points, both Andreae and Ramanathan (2013) and Chung et al. (2012) called

105 for model-independent, observation-based determination of the absorptive direct radiative forcing (ADRE) of aerosols. Since cloudiness and cloud type change on short time scales, long-term, highly time-resolved measurements covering different conditions, are necessary to unravel the role of absorbing aerosol on the HR.

Some satellite-based studies investigated the role of cloudiness and cloud type on the HR of aerosol layers above clouds (Matus et al., 2015). To our knowledge, there has been no experimental investigation on the impact aerosol

110 layers laying below the clouds, where conversely most of the aerosol pollution resides. This study was performed in Milan (Italy), located in the middle of the Po Valley (section 2), this region representing a pollution hotspot in Europe due to the high emissions coupled to a complex topology of the landscape. In fact, similarly to a multitude of basin valleys surrounded by hills or mountains in Europe, low wind speeds and stable atmospheric conditions are common, thus promoting high concentrations of aerosol and BC (Zotter et al., 2017; Moroni et al., 2013;

115 Moroni et al., 2012; Ferrero et al., 2011a ; Carbone et al., 2010; Rodriguez et al., 2007). At the same time, cloud

presence cannot be neglected considering that in the last 50 years annual mean cloudiness, expressed in oktas, is estimated to be ~5.5 over Europe (Stjern et al., 2009) and ~4 over Italy (Maugeri et al., 2001). This is in agreement with 80 years of data of cloud cover in the United States (Crock et al., 1999). Moreover, recently, Perlwitz and Miller (2010) reported a counterintuitive feedback linking the atmospheric heating induced by tropospheric

120 absorbing aerosol to a cloud cover increase.

Due to the aforementioned reasons, this study attempts to experimentally unravel for the first time the impact of different cloud types on the HR exerted by aerosol layers. To this purpose we use a methodology, previously developed in Ferrero et al. (2018), and further extended the analysis to explore the effects of different cloud types on BC and BrC on HR.. More in detail, with respect to the preliminary results by Ferrero et al. (2018), this work

125 introduces the following novelties: 1) the introduction of a cloud type classification; 2) the determination of the average photon energy impinging the absorbing aerosol; 3) the determination of the impact of both cloudiness and cloud types on the HR of BC and BrC; 4) the investigation of the relative and synergic role of cloudiness and of different cloud types on HR of both BC and BrC. The results presented in this study thus add an important piece of information in the general context of cloud - absorbing aerosol HR interactions

130

2   Methods

Aerosol clouds and spectral radiation measurements were carried in an experimental measurement station located on the rooftop (10 m above the ground level) of the U9-building of the University of Milano-Bicocca (45°30'38"N, 9°12'42"E, Italy; Figure 1). The site is located in the Po Valley in the midst of one of the most industrialized and

135 heavily populated area in Europe. In the Po Valley, stable atmospheric conditions often occur causing a marked seasonal variation of aerosol concentrations within the mixing layer, well visible even from satellites (Ferrero et al., 2019; Di Nicolantonio et al., 2009; Barnaba and Gobbi 2004). A full description of the aerosol behavior in Milan at the University of Milano-Bicocca and the related aerosol properties (vertical profiles, chemistry, hygroscopicity, sources, and toxicity) are reported in previous studies (Diemoz et al., 2019; D'Angelo et al., 2016;

140 Curci et al., 2015; Ferrero et al., 2015, 2010; Perrone et al., 2013; Sangiorgi et al., 2011). Within the framework of the present work is important to underline that the U9 experimental site is particularly well suited for atmospheric radiation transfer measurements, in fact it is characterized by a full hemispherical sky-view equipped with the instruments described in Section 2.1. The measurements assembly allow the experimental determination of the instantaneous aerosol HR (K day^{-1}) induced by absorbing aerosol (e.g. BC and BrC) as detailed in Section

145 2.2. The methodological approach used to quantify the cloud fraction and to classify the cloud type is instead reported in Section 2.3.

2.1   Instruments

At the U9 sampling site in Milan, the aerosol, cloud and radiation instrumentation (Figure S1) needed to determine

150 the HR (section 2.2), the cloud fraction and the cloud type (section 2.3) has been installed since 2015.

In particular, measurements of the wavelength dependent aerosol absorption coefficient $b_{abs(\lambda)}$ in the UV-VIS-NIR region were obtained using the Magee Scientific Aethalometer AE-31. The reason of this choice (detailed in Ferrero et al., 2018) is related to the number and range of spectral channels (7-λ: 370, 470, 520, 590, 660, 880 and 950 nm) not available in other instruments (e.g. MAAP, PSAP, photoacustic) (Virkkula et al., 2010; Petzold et al.,

155 2005). This spectral range is needed for the HR determination (section 2.2). It noteworthy that the Aethalometers

take also the advantage of global long-term data series (Ferrero et al., 2016; Eleftheriadis et al., 2009; Collaud-Coen et al., 2010; Junker et al., 2006) that should allow in the future to derive historical data of the HR.

To account for both the multiple scattering (the optical path enhancement induced by the filter fibers) and the loading effects (the non-linear optical path reduction induced by absorbing particles accumulating in the filter),
160   the AE-31 data were corrected applying the Weingartner et al. (2003) procedure (Ferrero et al., 2018, 2014, 2011; Collaud-Coen et al., 2010). As detailed by Collaud Coen et al. (2010), the Weingartner et al. (2003) procedure compensates for all the Aethalometer artifacts (the backscattering is indirectly included within the multiple scattering correction), showing a good robustness (negative values are not generated and results in good agreement with other filter photometers) and, most importantly, it does not affect the derived aerosol Absorption Angstrom
165   Exponent (AAE) (fundamental for HR determination, section 2.2).

Overall, the multiple scattering parameter C was 3.24±0.03 as obtained by comparing the AE31 data at 660 nm with a MAAP at the same wavelength (Figure S2). This value lies very close to that suggested by GAW (2016), i.e. C=3.5. The loading effects were dynamically determined following the Sandradewi et al. (2008b) approach while the final equivalent BC concentrations (eBC) were obtained applying the AE-31 apparent mass attenuation
170   cross-section (16.6 m^2 g^{-1} at 880 nm).

Radiation measurements ($F_{n(\lambda,\theta)}$) were collected using a Multiplexer-Radiometer-Irradiometer (MRI) (Figure S1). The MRI resolves the UV-VIS-NIR spectrum (350 - 1000 nm) in 3648 spectral bands for both the downwelling and the upwelling radiation fluxes. The MRI was equipped with a rotating shadow-band enabling to measure separately the spectra of the direct, diffuse and reflected radiation.
175   The reflected radiation originated from the Lambertian concrete surface(due to its flat and homogeneous characteristics which well represents the average spectral reflectance of the Milano urban area; Ferrero et al, 2018). Details of the MRI are reported in Cogliati et al. (2015).

Broadband downwelling (global and diffuse) and upwelling (reflected) radiation measurements were also collected using LSI-Lastem radiometers (DPA154 and C201R, class1, ISO-9060, 3% accuracy; 300-3000 nm). Diffuse
180   radiation was measured using the DPA154 global radiometer equipped with a shadow band whose effect was corrected (Ferrero et al., 2018) to determine the true amount of both diffuse and direct (obtained after subtraction from the global) radiation.

In addition to radiation measurements, temperature, relative humidity, pressure and wind parameters were measured using the following LSI-Lastem sensors: DMA580 and DMA570 for thermo-hygrometric measurements
185   (for T and RH: range -30 - +70 °C and 10% - 98%, accuracy of ± 0.1 °C and ± 2.5% sensibility of 0.025°C and 0.2%), the CX110P barometer model for pressure (range 800-1100 hPa, accuracy of 1 hPa) and the combiSD anemometer (range of 0 - 60 m/s and 0-360°) for wind.

The experimental station U9 is also equipped with an Automatic Lidar-Ceilometer (ALC) operated by ISAC-CNR in the framework of the Italian Automated LIdar-Ceilometers network (ALICENET, www.alice-net.eu) and
190   contributing to the EUMETNET E-Profile ALC Network (https://www.eumetnet.eu/). It is a Jenoptik Nimbus 15k biaxial lidar-ceilometer operating 24 hours per day, 7 days per week. It is equipped with a Nd:YAG laser that emits light pulses at 1064 nm with an energy of 8 μJ per pulse and a repetition rate of 5 kHz. The backscattered light is detected by an avalanche photodiode in photon counting mode (Wiegner & Geiß, 2012). The vertical and temporal resolution of the raw signals are 15 m and 15 seconds, respectively. Signals are recorded up to 15 km
195   height, with an overlap height < 1000 m. Vertical signals are averaged at 120 seconds to improve the signal to

noise ratio. The Nimbus 15k lidar-ceilometer is able to determine cloud base heights, penetration depths, mixing layer height and, with specific processing, vertical profiles of aerosol optical and physical properties (e.g., Haeffelin et al., 2011, Dionisi et al., 2018; Diemoz et al., 2019a, 2019b). For the specific purpose of this study, exploitation of the U9 ALC data has been limited to cloud layering and relevant cloud base height as the system

200   can reliably detect multiple cloud layers and cirrus clouds (Boers et al., 2010; Martucci et al., 2010; Wiegner et al., 2014) within its operating vertical range (up to 15 km).

Global and diffuse radiation measurements, coupled with the ALC data were used to determine the sky cloud fraction and to classify the cloud types by following the methodology presented in the Section 2.3.

205   **2.2   Heating rate measurements**

The instantaneous aerosol HR (K day^{-1}) induced by absorbing aerosol is experimentally obtained following Eq. 1 using the methodology reported and validated in Ferrero et al. (2018). Here we briefly summarize the method and the reader is referred to the aforementioned publication for the physical demonstration of the approach.

The integral over the whole shortwave solar spectrum and over the whole 2π hemispherical sky of the interaction

210   between the radiation (either direct from the sun, diffuse by atmosphere and clouds and reflected from the ground) and the absorbing components of aerosol (BC and BrC in Milan, as detailed in Ferrero et al., 2018) gives the HR as:

$$HR = \frac{1}{\rho C_p} \cdot \sum_{n=1}^{3} \int_\theta \int_\lambda \frac{F_{n(\lambda,\theta)}}{\mu} b_{abs(\lambda)} d\lambda \, d\theta \tag{1}$$

where ρ represents the air density (kg m^{-3}), C_p (1005 J kg^{-1} K^{-1}) is the isobaric specific heat of dry air, n is the

215   index indicating the nth type of radiation (direct, diffuse or reflected) impinging the absorbing aerosol, λ and θ represent the wavelength and zenith angle of the radiation, $F_{n(\lambda,\theta)}$ is the nth type (direct or diffuse or reflected) monochromatic radiation of wavelength λ that strikes with an angle θ the aerosol layer, μ is the cosine of θ (cosθ), $b_{abs(\lambda)}$ is the wavelength dependent aerosol absorption coefficient.

Considering that the absorptive DRE (ADRE), i.e. the radiative power absorbed by the aerosol for unit volume of

220   the atmosphere (W m^{-3}), is equals to:

$$ADRE = \sum_{n=1}^{3} \int_\theta \int_\lambda \frac{F_{n(\lambda,\theta)}}{\mu} b_{abs(\lambda)} d\lambda \, d\theta \tag{2}$$

Eq. 1 can be also re-written as:

$$HR = \frac{1}{\rho C_p} \cdot ADRE \tag{3}$$

Both Eq. 1 and 2 can also be solved for each of the three components of radiation (direct, diffuse, or reflected),

225   i.e.:

$$HR = HR_{dir} + HR_{dif} + HR_{ref} \tag{4}$$

$$ADRE = ADRE_{dir} + ADRE_{dif} + ADRE_{ref} \tag{5}$$

where the subscript *dir*, *dif* and *ref* refers to the direct, diffuse and reflected radiation, respectively.

Eq. 4 and 5 allow to split the total ADRE and HR into the three components of radiation. As the intensity of these

230   radiation components is a function of cloudiness and cloud type (section 2.3), Eqs. 4 and 5 enable to assess the impact of the latter components on the aerosol absorption of shortwave radiation and thus on the corresponding HR (sections 3.2 and 3.3).

In addition, as the spectral signature of $b_{abs(\lambda)}$ reflects the different nature of absorbing aerosol (BC and BrC), $b_{abs(\lambda)}$ and thus the HR can be apportioned to determine the contributions of BC and BrC (HR$_{BC}$ and HR$_{BrC}$), respectively.

235 This result can be achieved considering that BC aerosol absorption is characterized by an Absorption Angstrom Exponent, AAE $\approx$1 (Massabò et al., 2015; Sandradewi et al., 2008a; Bond and Bengstrom, 2006). Conversely, BrC absorption is spectrally more variable, with an AAE from 3 to 10 (Ferrero et al., 2018; Shamjad et al., 2015; Massabò et al., 2015; Bikkina et al., 2013; Yang et al., 2009; Kirchstetter et al., 2004). This is due to the negligible BrC absorption in the infrared compared to UV. In this study we determined AAE$_{BrC}$ following the innovative

240 apportionment method proposed by Massabò et al. (2015). This allows to apportion $b_{abs(\lambda)}$ from BC and BrC at the same time and to determine the AAE$_{BrC}$ assuming that the whole BrC is completely produced by biomass burning. The method by Massabò et al. (2015) was successfully applied to the Milan U9 measurements leading to an average AAE$_{BrC}$ (over a full solar year) of 3.66±0.03, and to an associated HR$_{BrC}$ explaining 13±1% of the total HR (Ferrero et al., 2018). The apportionment of absorption coefficient also enables to investigate the role of clouds

245 on different absorbing aerosol species. As already pointed out in Ferrero et al. (2018), it is worth recalling that in the present method (equation 1), both the ADRE and the HR are independent from the thickness (Δz) of the investigated atmospheric aerosol layer. At the same time, BC and HR vertical profiles data previously collected both at the same site and in other basin valley sited (Ferrero et al., 2014) revealed that ADRE and HR were constant inside the mixing layer, The methodology is therefore believed to be valid for applications in atmospheric layers

250 below clouds, assuming that near-surface measurements are representative of the whole mixing layer. Main advantage of the new method to quantify the impact of clouds on the LAA HR is that it allows to obtain experimental measurement (not estimations) of ADRE and HR, which are continuous in time and resolved in terms of sources, species of LAA, cloud cover, and cloud types.

255 ## 2.3 Cloud fraction, cloud classification and average photon energy

2.3.1 Cloud fraction

The cloud fraction was determined following the approach reported in Ehnberg and Bollen (2005). In particular, radiometer measurements were used to calculate the fraction of the sky covered by cloud in terms of oktas (N), overall leading to 9 classes, corresponding to values of N ranging from 0 (clear sky) to 8 (complete overcast

260 situation). As reported in Ehnberg and Bollen (2005), the amount of global radiation (F_{glo}) can be related to the solar elevation angle ($\pi/2-\theta$) and to the cloudiness condition following the Nielsen et al. (1981) equation:

$$F_{glo-N} = \left[\frac{a_0(N) + a_1(N)\sin\left(\frac{\pi}{2}-\theta\right) + a_3(N)\sin^3\left(\frac{\pi}{2}-\theta\right) - L(N)}{a(N)} \right] \tag{6}$$

where N represents one of the possible 9 classes of cloud fraction and a, a_0, a_1, a_3 and L are empirical coefficients that enable to compute the expected global radiation for each oktas class (F_{glo-N}), at a fixed solar elevation angle

265 ($\pi/2-\theta$). Their values, extracted from the original work of Ehnberg and Bollen (2005), are summarized in Table S1. Eq. 6 allows to determine the unique oktas value N by comparing the measured global radiation (F_{glo}) with F_{glo-N} at any given time.

Still, the so-derived cloud fraction can be used to evaluate the interaction between incoming radiation and light absorbing aerosol in cloudy conditions but without the possibility to discriminate between cloud type. The

270 following sections (2.3.2 and 2.3.3) describe the methods applied to overcome this limitation by implementing a cloud classification scheme.

2.3.2 Cloud classification

Cloud classes and cloud cover is by common practice still largely determined on the basis of human observations

275 based on the reference standard defined by the World Meteorological Organisation (WMO). However, these observations lack high time resolution information and are subjective. Due to high spatial and temporal variability of clouds, determination of cloud classes can be improved by measurements, adding highly temporally resolved and observer-independent information on the cloud base height and the magnitude of solar radiation.

In this study, clouds were classified coupling measurements of broadband solar radiation (global irradiance, F_{glo})

280 and lidar-ceilometer measurements. The full methodology is described below.

As first introduced in the study by Duchon & O'Malley (1999), measurements of the magnitude of global solar irradiance and its deviation in 20-minute intervals can be used for cloud classification. Irradiance is used to calculate two quantities: 1) the ratio (R) between observed global irradiance (F_{glo}) and the modelled clear sky irradiance (GHI) (Robledo and Soler, 2000) expected at the same time and place (also referred to as scaled

285 irradiance) and 2) the standard deviation (SD) of the measured global irradiance in 20 minute time intervals. Following the work of Duchon & O'Malley (1999), the SD-R plot enables to distinguish different cloud categories: clear sky conditions (CS), Stratus (St), Cirrus clouds (Ci) and cumulus (Cu). Figure 2a-h shows an example of the temporal evolution of the observed F_{glo}, F_{dif} and GHI, together with the corresponding SD-R diagrams for the aforementioned 4 cloud classes identified by Duchon & O'Malley (1999). In a CS case (Figure 2a), F_{glo} approaches

290 GHI without any significant temporal variation, thus leading to a R close to 1 and SD close to 0 W m^{-2} (Figure 2b). Conversely, St clouds suppress the incoming radiation (Figure 2c) for all the time related to their presence resulting in R and SD both approaching 0 (Figure 2d) allowing a complete separation from the CS case. Ci clouds (Figure 2e) moderately suppress F_{glo} with smoothed fluctuations in time leading to a R between 0.75 and 1 and a SD ranging from 0 to ~100 W m^{-2} (Figure 2f); Ci clouds region thus lies adjacent but separated from the CS one.

295 Finally the last case study (Figure 2g) shows a transition from CS (before midday) to Cu clouds in the afternoon; the arrival of Cu clouds in the sky first scattered R around 1 (Figure 2h; both below and slightly above it in keeping with Mims and Frederick (1994) and Feister et al. (2015)) and, most important, SD increased from 100 up to 500 W m^{-2} due to the Cu clouds movement in the sky which results in fast sun/shadows transitions. As a consequence, the Cu clouds regions is wider and above the one of Ci clouds. More recently, Harrison et al. (2008), went deeper

300 showing that the SD-R differentiates between St and stratocumulus (StCu) clouds as StCu clouds are characterized by R values mostly moving from 0.4 to 0.8 and SD between 0 and 200 W m^{-2}. In this respect, StCu clouds can be found in the middle region of the SD-R space, with different levels of SD, depending on the cumuliform condition. As a consequence, despite the promising classification introduced by Duchon & O'Malley (1999) and Harrison et al. (2008), by using the SD-R diagram alone it is possible to encounter episodes of misclassification, especially

305 because it is impossible to retrieve information concerning the contemporary presence of different cloud levels from the SD-R diagram alone. Therefore, the cloud classification was further improved in this study by including information from the automated Lidar-Ceilometer measurements on the cloud base height and the number of cloud layers. First of all, to avoid misclassification cases due to the presence of multiple cloud layers, we limited the analysis to those cases where only one cloud layer was detected by ceilometer (ALC). In this respect, the ALC-

310 derived cloud base height information allowed us to cluster clouds according to their altitude and distinguishing between low level clouds (<2 km), mid-altitude clouds (2-7 km) and high-altitude clouds (>7 km). The cloud

altitude of each analyzed data is reported in Figure 3 within the SD-R diagram. It shows that, on average, low level clouds are located on the left side of the SD-R diagram(stratiform clouds), high-altitude clouds are conversely on the opposite side (this being the the region of Ci and Cu clouds); finally, mid-altitudes clouds density in the diagram

315   mostly cover its the central part describing all the possible transitions/combinations from St to Cu and Ci, e.g. altostratus (AlSt) altocumulus (AlCu). Figure 3

further shows that use of the clouds base height as a third source of information (in addition to R and SD) allows to better separate overlapping cases in the bi-dimensional, SD-R diagram alone.

Overall, coupling the SD-R plot and cloud base height, enabled us to identify seven classes: St (stratus), Cu

320   (cumulus) and StCu (stratocumulus) as low level class; AlSt (altostratus) and AlCu (altocumulus) as mid-altitude clouds; and Ci (cirrus) and CiCu-CiSt (cirrocumulus and cirrostratus) as high-altitude clouds. The final overview of the parameters (R, SD, cloud level) and their threshold values used for cloud classification is presented in Table 1. The final SD-R diagram with presentation of mean value and 99% confidence interval for R and SD of each cloud class, plus the clear sky (CS) case, is presented on Figure 4 while the same SD-R diagram with presentation

325   of mean value and the standard deviation of each cloud classes, plus the clear sky (CS) case, is presented on Figure S3. Note in particular that the overlapping in the standard deviation of each classes shown in the SD-R plot in Figure S3 are solved by the introduction of the cloud base height from lidar data underling the reliability of the performed cloud classification. Final cloud classification was obtained for the period from November 2015 - March 2016, during which all necessary parameters were available (section 3).

330

2.3.3 Average photon energy

The relative distribution of energy over the solar spectrum in the measured range of the MRI (350 - 1000 nm) was also investigated for each cloud type calculating the average photon energy (APE) which describes the spectral characteristics of direct and diffuse radiation modulated by clouds. In fact APE quantifies the spectral shape of

335   solar irradiance and represents the average energy of photons impinging upon a target, in this case the aerosol layer close to the surface. Thus, single APE can identify a unique spectral irradiance distribution which describes the light available for absorption in different spectral regions. APE (expressed in eV) is calculated dividing the total energy in a spectrum by the total number of photons it contains (Norton et al., 2015), i.e.:

$$APE_n = \frac{1}{q}\left[\frac{\int F_{n,\lambda} d\lambda}{\int \Phi_\lambda d\lambda}\right] \tag{7}$$

340   where q represents the electron charge, $F_{n,\lambda}$ is the nth type (direct, diffuse) radiation at wavelength λ (W m^{-2} nm^{-1}), and Φ_λ (photons m^{-2} s^{-1} nm^{-1}) is the photon flux density at wavelength λ determined using the Plank-Einstein equation:

$$\Phi_\lambda = \frac{F_{n,\lambda}}{hc/\lambda} \tag{8}$$

where h is the Plank constant and c the speed of light.

345   From Eq. (8) it follows that APE is normalized for the total amount of radiation, becoming thus independent from the absolute intensity of light at each λ and indicating only the average distribution of light across the spectrum. Particularly, higher APE values describe the shift of a radiation spectrum towards UV-blue region (Figure S4). It has to be noted that the APE index depends on the range of the investigated spectrum (lower and upper limits of

the integral), which in our case relate to the MRI measurements (350 - 1000 nm), thus for any absolute APE
comparison with other studies, the spectrum range should be taken into account.

350

Characteristic APE values of diffuse (APE$_{diff}$) and direct (APE$_{dir}$) irradiance measured from U9 site for different
sky condition are presented in Section 3.4 together with a discussion concerning the relationship between APE
and HR.

3   Results and Discussion

355

HR values considered in this study were measured over Milan from November 2015 to March 2016 are, as this
period covers the simultaneous presence of radiation, lidar and absorption measurements fundamental for the
analysis presented here (section 2). These data are presented in Section 3.1. The role of cloudiness and its influence
on the HR is discussed in section 3.2 while section 3.3 describes the impact of each cloud type on the HR. In

360

Section 3.4, the clouds impact on the HR is discussed with respect to the light absorbing aerosol species: BC and
BrC. All the data are reported everywhere as mean±95% confidence interval.

3.1   HR, eBC and radiation data

Monthly average values of eBC and HR are presented in Figure 5a while the corresponding numerical values of

365

these and additional parameters (e.g. ADRE, b$_{abs}$) are also summarized in Table 2. Corresponding high time
resolution data (5 minutes) are shown in Figure S5.

The highest values of eBC (and $b_{abs(880nm)}$) were found, as expected, in the middle of the winter, in December
(6.29±0.09 μg m^{-3} and 31.1±0.5 Mm^{-1}, respectively) when strong emissions in the Po Valley are released into the
stable boundary layer (Sandrini et al., 2014; Ferrero et al., 2011b; Barnaba et al., 2010). In fact, in this month the

370

average PM$_{10}$ and PM$_{2.5}$ were also at their maximum, with 73.1±0.6 and 69.3±0.6 μg m^{-3}, respectively (source:
Milan Environmental Protection Agency, ARPA Lombardia). Thus, eBC accounted for ~10% of PM mass
concentration, resulting in the absorption of shortwave radiative power (ADRE) of 20.7±0.7 mW m^{-3} which was
responsible for an HR of 1.43±0.05 K day^{-1}. The lowest HR (monthly average) was recorded in spring (March)
with a value of 0.54±0.02 K day^{-1} related to an amount of eBC of 1.54±0.04 μg m^{-3}.

375

These values of eBC, HR and ADRE agree with those observed previously in the Po Valley (Ferrero et al., 2014,
2018) and confirm that eBC is the main driver for the behavior of HR and ADRE on the seasonal time scale.
However, in agreement with Eq. 1 (section 2.1), the interaction of absorbing aerosol with the impinging radiation
cannot be neglected as heating rate varies differently than anticipated from the concentrations alone. In fact, during
the investigated period, the ratio between maximum and minimum eBC monthly mean concentration (December

380

to March, eBC ratio: 4.10±0.12) was higher than that of HR (2.65±0.16). This is because the incoming radiation
was lower in December (F_{glo}: 141±4 W m^{-2}; Figures 5b and S5) with respect to March (F_{glo}: 310±7 W m^{-2}, ratio
of 0.45±0.02), partially compensating the marked wintertime increase of eBC. This is mainly due to the interaction
of light absorbing aerosol with F_{dir}. In fact, once F_{dir} is scaled by μ (eq. 1, section 2.1, Figure S6) it is quite constant
along the year (and perfectly constant only in clear sky conditions). Conversely, the diffuse and reflected radiation

385

(Figure S6), even when scaled by μ (under the isotropic and Lambertian assumptions), linearly follow the behavior
of irradiance F_{dif} and F_{ref} thus being seasonally modulated (Figure S6). A detailed discussion about this explanation
is reported in Ferrero et al. (2018).

These considerations introduce the importance of both amount and kind (direct, diffuse and reflected) of the radiation that interacts with light absorbing aerosol. In brief, any process able to influence the total amount and

390 the kind of impinging radiation (e.g. presence/absence of clouds, cloudiness and cloud type) will result in a different HR, even keeping constant eBC levels. The investigation of this aspect is the main focus and added value of this study and is reported in the next sections.

3.2 Cloud fraction impact on the hating rate

395 The first indication of the important role played by clouds on the HR can be derived from the contribution of the diffuse radiation to the HR (HR_{dif}) as reported in Figure 5a. It shows the monthly average values of HR, HR_{dir}, HR_{dif} and HR_{ref} revealing that the diffuse contribution accounted for 40±1% of the total HR. On a monthly basis, this was comparable or even higher than HR_{dir}. The only exception was in November 2015 were a lower fraction of diffuse radiation was measured (Figure 5b) compared to the other months. In fact, in November, the average

400 okta value was 2.91±0.06, lower than that observed in the other months (3.75±0.03), due to the highest frequency of clear sky conditions. The aforementioned data demonstrate the importance of diffuse radiation and thus of cloudy days in determining the HR induced by the absorbing aerosol. In order to investigate the role of cloudiness, it is necessary to decouple the variability of the HR induced by radiation from that due to eBC concentrations. In Figure 6 we thus show how fast a volume of air containing a specific BC mass heats due to the absorption of the

405 impinging radiation – that is, HR values normalized to the unit mass of eBC (K m^3 day^{-1} μg^{-1}) – as a function of oktas and further differentiate its components (HR_{dir}/eBC, HR_{dif}/eBC) as well as radiation (F_{dir} and F_{dif}). HR_{dir}/eBC decreased constantly from clear sky conditions (okta=0) to complete overcast situation (oktas=7-8) following the decreasing amount of the incoming solar F_{dir}. At oktas values of 7-8, the HR_{dir} reached values close to 0. Conversely, HR_{dif}/eBC increased with increasing cloudiness, but not continuously. In fact, HR_{dif}/eBC showed a

410 maximum peak (0.16±0.01 K m^3 day^{-1} μg^{-1}) at intermediate cloudiness conditions (5-6 oktas) when also the diffuse radiation peaked reaching F_{dif}: 147±6 W m^{-2}, doubling the relevant value in completely overcast conditions (74±3 W m^{-2}; 7-8 oktas) and exceeding 150% of that in clear sky (91±2 W m^{-2}). In overcast situations (oktas=7-8) both HR_{dif}/eBC and the diffuse radiation reached their minimum due to the capability of clouds to effectively attenuate the radiation. Yet, differently from the direct radiation, the HR_{dif}/eBC is still not null (0.08±0.01 K m^3 day^{-1} μg^{-1})

415 becoming the highest contributor of the total atmospheric HR, with a percentage of 84±1%.

The absolute values of the HR and its components as a function of cloudiness is shown in Figure 6b. We show seasonally averaged (winter: NDJ, spring: FM) HR in clear sky (oktas=0) and complete overcast situation (oktas=7-8). In clear sky, the direct component of the HR (HR_{dir}) was higher than HR_{dif} and HR_{ref} accounting for 1.35±0.04 K day^{-1} and explaining on average 60±5% of the total HR during winter. Similarly, in clear sky

420 springtime conditions, HR_{dir} was 0.47±0.01 K day^{-1} again higher than HR_{dif} and HR_{ref}. Conversely, in complete overcast conditions (Oktas=7-8), HR_{dif} alone (84±1% of total HR) accounted for 0.33±0.01 and for 0.19±0.01 K day^{-1} during winter and spring, in agreement with Figure 5a.

These results highlight that clouds are responsible for an important feedback on the aerosol HR that needs to be carefully quantified, pointing to the need to correctly include and model cloudy conditions in radiative transfer

425 calculations of the 'real world' aerosol DRE and the HR.

Experimental HR measurements at high-time resolution hence enable us to estimate the degree of error introduced by improperly assuming clear-sky conditions in radiative transfer calculations. Particularly, we found that by

incorrectly assuming clear-sky conditions the HR of light absorbing aerosol can be overestimated by the following factors: 50% (low cloudiness, oktas=1-2), 109% (moderate cloudiness, oktas=3-4), 148% (intermediate

430   cloudiness, oktas=5-6) and 470% in cloudy conditions (oktas=7-8). Note that, during the campaign, clear sky conditions were present only 23% of the time, the remaining time (77%) being characterized by partially cloudy (35%, 1-6 oktas) to totally cloudy (42%, 7-8 oktas) conditions.

3.3   Cloud type impact on the heating rate

435   The previous section showed the importance of cloudiness in determining both the kind of the active radiation and the suppression of HR with increasing the cloud cover. This is relevant as it was found that cloudy conditions are dominant in terms of frequency. Here we will further investigate the clouds-HR relationships by exploring the effect of different types of clouds on this relationship. Figure 7a shows how the overall 77% of cloudy conditions encountered during the observational period was composed by the different cloud types, revealing that these were

440   mainly St (42%), followed by StCu (13%) Ci, CiCu-CiSt (7% and 5%, respectively). The contribution of each cloud type to the cloudiness (expressed in oktas) of the sky is reported in Figure 7b. This clearly shows that, while St were mostly responsible of overcast situations (oktas=7-8, frequency: 87 and 96%), StCu dominated the intermediate cloudiness conditions (oktas=5-6, frequency: 47 and 66%); moderate cloudiness (oktas=3-4) were mostly due to a transition from CiCu-CiSt to StCu while low cloudiness (oktas=1-2) were mostly dominated by

445   Ci and Cu (frequency: 59 and 40%, respectively). The impact of each cloud type on the HR/eBC and F_{glo}, together with the corresponding components (HR$_{dir}$/eBC and F_{dir}; HR$_{dif}$/eBC and F_{dif} ; HR$_{ref}$/eBC and F_{ref}) is reported in Figure 8a-d. The figure shows a prefect agreement between cloud radiation suppression of different cloud types and the consequent HR decrease (R^2>0.93; not shown). It also highlights how critical is, for radiative transfer calculations and HR determination, to conduct a proper simulation taking into account the role of each cloud type.

450   We see that roughly, all different cloud types reduce HR/eBC differently, while their influence on the diffuse component HR$_{dif}$/eBC is less diverse. In terms of absolute values (not normalized for eBC), Figure 9 reveals that the HR due to direct radiation was only dominant during CS and Ci conditions (HR$_{dir}$: 1.11±0.04 and 0.92±0.05 K day^{-1}, respectively), explaining 66±3 and 57±4% of the total atmospheric HR of light absorbing aerosol (LAA). In the other cloudy cases (St, AlSt and StCu) HR$_{dif}$ dominates, reaching the highest absolute contribution of

455   84.4±3.8, 83.0±10.7 and 76±4% (HR$_{dif}$: 0.25±0.01, 0.34±0.03 and 0.66±0.02 K day^{-1}), respectively.
Exploring the relationship between cloud type and HR, we found a strong linear relationship between the mean cloudiness (in oktas) and the percent decrease of HR due to each cloud type with respect to the clear sky (CS) case (Figure 10). These results were obtained by averaging the cloudiness (in oktas) for each cloud type (as detected in section 3.3) and computing the cloud-type resolved percentage decrease of LAA HR with respect to clear sky

460   conditions. Overall, the derived linear regression (R^2=0.96) indicates a HR decrease of about 12% per okta. Knowledge of the dominant cloud types associated to the different cloud cover also allows us to associate this decrease to specific cloud types (Figure 10). In particular, Ci are found to produce a modest impact on cloudiness (0.50±0.05 oktas) decreasing the HR by ~3%, while Cu (1.76±0.09 oktas) decrease the LAA HR by -26±8%. CiCu-CiSt (oktas of 3.56±0.14) were responsible for a -49±6 decrease of the HR. Their impact was comparable to

465   that of StCu (4.68±0.10 oktas, -48±4% of HR). AlCu (4.11±0.18 oxtas) had a higher impact, decreasing the HR of -59±6%. The highest impact was given by AlSt (6.57±0.15 oktas; -76±4% of HR) and finally by St (oktas: 7.19±0.04) that suppressed the LAA HR by a factor of -83±4%.

It is also worth to mention that not only the absolute value of the HR changes as a function of clouds in the atmosphere, but the presence of clouds also alters its diurnal pattern. In fact, as introduced in section 3.1, F_{dir} is

470 scaled by μ in Eq. 1 (section 2.1) and thus it is perfectly constant along the day only in clear sky conditions. Conversely, even when scaled by μ, the diffuse and reflected radiation linearly follow the behavior of irradiance F_{dif} and F_{ref} (under the assumption of isotropic and Lambertian surface, Ferrero et al., 2018).

Thus any influence of clouds on F_{dir}, F_{dif} and F_{ref} will reflect into the interaction between the radiation itself and the absorbing aerosol, changing the HR diurnal pattern . To illustrate this effect, Figure 11 shows the average

475 diurnal pattern of the HR in both clear sky (blue) and cloudy conditions (red; oktas=7-8, dominated exclusively by St and AlSt). This clearly shows that, while in clear sky conditions the HR exhibits an asymmetric diurnal pattern with a maximum around 10:00 LST, in cloudy conditions it shows a bell shape curve similar to that of F_{glo} (which is driven by the diffuse only component, which peaks at midday). As explained in more detail in Ferrero et al. (2018), the presence of the asymmetrical peak in clear sky conditions is due to the coupling between the eBC

480 daily pattern (characterized by a morning rush hour peak) and that of F_{dir}/μ, that is constant in CS. This is not the case in cloudy conditions when the most important radiation is F_{dif}.

A further important consequence of that change in the diurnal pattern of HR is that it reflects into related atmospheric feedbacks, such as the influence on the liquid water content (Jacobson et al., 2002), planetary boundary layer dynamics (Ferrero et al., 2014; Wang et al., 2018), regional circulation systems (Ramanathan and

485 Carmichael, 2008; Ramanathan and Feng, 2009) and finally on the cloud dynamic and evolution itself (Koren et al., 2008; Bond et al., 2013). Thus, any inappropriate use of clear sky assumption in models will also reflect on the modelled HR-triggered feedbacks.

3.4   The impact of clouds on the absolute and relative BC and BrC heating rates

490 As mentioned in the introduction, one of the key uncertain factors in climate change evaluations is the role played by different species of absorbing aerosol, the two most important species being BC and BrC. In this work we thus investigate the contribution of these two species to the HR at our measuring site. In the previous sections we discussed the absolute intensity of HR_{BC} and HR_{BrC}. They varyis function of four main variables, namely: 1) the absolute absorption coefficient values ($b_{abs(\lambda)}$) of both BC and BrC, 2) the absolute magnitude of the impinging

495 radiation ($F_{n(\lambda,\theta)}$), 3) the different spectral absorption of BC and BrC, described by their AAE, and 4) the spectral features of the impinging radiation ($F_{n(\lambda,\theta)}$) described by the APE (section 2.3.3). Among these factors, the first two are the dominant ones. However, the presence of clouds influences both the absolute magnitude and the spectral feature of the impinging radiation (sections 3.2 and 3.3).

We first present the impact of cloudiness and cloud type on both HR_{BC} and HR_{BrC} considering the absolute values

500 of $b_{abs(\lambda)}$ and $F_{n(\lambda,\theta)}$ measured during the campaign (section 3.4.1). Then, in Section 3.4.2, we discuss the influence of different sky conditions and cloud type on HR due to both BC and BrC, focusing on the radiation APE through a HR_{BC} and HR_{BrC} data normalization with respect to the absolute magnitude of the $b_{abs(\lambda)}$ of both species.

3.4.1   The role of cloudiness

505 To complement the results in Figure 5a, the contribution of BC and BrC to the monthly averaged HR is reported in Figure 12. On average, the HR_{BrC} accounted for 13.7±0.2% of the total HR, the BrC being characterized by an AAE of 3.49±0.01, thus fully within ranges previously observed in other studies (e.g., Yang et al, 2009; Massabò

et al., 2015; Ferrero et al., 2018). In Figure 13, HR_{BC} and HR_{BrC} are reported as a function of the oktas (total HR in Figure 13a and the contribution of direct, diffuse and reflected HR in panels b-d, respectively). As expected,

510 Figure 13a shows that both HR_{BC} and HR_{BrC} decreased with increasing oktas, going from the clear sky maxima (HR_{BC} and HR_{BrC}: 1.14 ± 0.03 and 0.20 ± 0.01 K day^{-1}) to the overcast conditions minima (mainly due to St and AlSt clouds; see Figure 7b) of 0.16 ± 0.01 and 0.02 ± 10^{-3} K day^{-1}, respectively. This change is an important result related to the decrease of the absolute magnitude of impinging radiation, as described in sections 3.2 and 3.3. In fact, during the campaign, clear sky conditions were present only 23% of the time, the remaining time (77%) being

515 characterized by partially cloudy (35%, 1-6 oktas) to totally cloudy (42%, 7-8 oktas) conditions. Moreover, as reported in the same sections (3.2 and 3.3) and shown in Figures 5 and 6, the change of radiation magnitude with cloudiness was different for direct, diffuse and reflected radiation. This behavior affected the corresponding direct, diffuse and reflected radiation components of HR_{BC} and of HR_{BrC} (Figure 13 b-d). For the direct radiation, Figure 13b shows both $HR_{BC,dir}$ and $HR_{BrC,dir}$ to decrease as a function of cloudiness to negligible levels (HR<10^{-4} K day^{-}

520 ^{1}) in overcast conditions. Conversely, $HR_{BC,dif}$ and $HR_{BrC,dif}$ increased for increasing oktas (Figure 13c), reaching their maximum in partially cloudy conditions (at oktas=6, 0.51 ± 0.01 and 0.09 ± 0.01 K day^{-1}) when also the maximum of F_{dif} was registered (section 3.2 and Figure 6a). Then, for further increasing cloudiness, they dropped down to minimum values (0.13 ± 0.01 and 0.02 ± 0.01 K day^{-1}). Finally, $HR_{BC,ref}$ and $HR_{BrC,ref}$ (Figure 13d) behave similarly to the total HR_{BC} and HR_{BrC}, being the reflected radiation dominated by the total radiation impinging on

525 the ground (see Figures 8a and 8d for a comparison). In this respect, $HR_{BC,ref}$ and $HR_{BrC,ref}$ decreased with increasing oktas from maximum values in clear sky ($HR_{BC,ref}$ and $HR_{BrC,ref}$: $0.17\pm4*10^{-3}$ and $0.03\pm1*10^{-3}$ K day^{-1}) down to overcast minimum ($HR_{BC,ref}$ and $HR_{BrC,ref}$ 0.02 ± 10^{-3} and $3*10^{-3}\pm10^{-3}$ K day^{-1}).

Figure 13 also clearly shows that HR_{BC} is always greater than HR_{BrC}, as expected. However, a deeper investigation of the data reported in Figure 13 allows us to better describe the interaction between radiation and LAA in heating

530 the surrounding atmosphere. To this purpose, it is particularly useful to compare the relative decrease of HR_{BrC} from clear sky to complete overcast situation to that of HR_{BC}. The clouds, going from 0 to 8 oktas, decrease the HR_{BrC} $12\pm6\%$ more compared to HR_{BC}. The same happened to $HR_{BC,dir}$ and $HR_{BrC,dir}$. The diffuse component of the HR behaves differently: the clouds decrease $HR_{BrC,dif}$ $38\pm6\%$ more compared to $HR_{BC,dif}$.

At a first glance, Figure 13 could give the impression that BrC is more efficient in heating the surrounding

535 atmosphere (with respect to BC) in clear sky conditions, compared to cloudy ones. Note however that, as stated at the beginning of this section, any change of both BC and BrC $b_{abs(\lambda)}$ in different sky conditions has to be accounted for to avoid any misinterpretation of the results.

In fact, we observed that at all wavelengths and for both BC and BrC, $b_{abs(\lambda)}$ was not constant during periods with different cloudy conditions (Figure S7). However, while the variability of $b_{abs(\lambda)}$ BC with varying oktas was limited,

540 this was not the case for BrC (Figure S7a).Values of $b_{abs(\lambda)}$ BrC in high cloud cover conditions were statistically lower than the one in clear sky/moderate cloudy conditions (at oktas=8 the $b_{abs(\lambda)}$ of BrC was on average $-23\pm3\%$ lower than in clear sky, Figure S7b). The full understanding of this behavior, perhaps linked to the formation of secondary BrC at high radiation in clear sky compared to cloudy ones (Kumar et al., 2018), is beyond the aim of the present paper. Here we focus the attention on the fact that the magnitude of $b_{abs(\lambda)}$ of BC and BrC changed

545 differently with cloudiness. This behavior explains why, at a first glance, the relative decrease of the HR_{BrC}, from 0 to 8 oktas, was higher compared to that of HR_{BC}. At the same time, the fact that the diffuse component of the HR_{BrC} ($HR_{BrC,dif}$) experienced a higher relative decrease (from clear sky situation to overcast ones) than those

observed for the total HR_{BrC} asks for further investigation. Some insights into this behavior are given in the next Section.

550

3.4.2   The role of the average photon energy and cloud type

In order to decouple the variability of the HR induced by radiation from that due to $b_{abs(\lambda)}$, both HR_{BC} and HR_{BrC} were normalized for the adimensional integral of the $b_{abs(\lambda)}$ over the whole aethalometer spectrum. In this way, the magnitude of $b_{abs(\lambda)}$ is accounted for along the whole spectrum avoiding the choice of an arbitrary λ as a reference

555   for the normalization. Figure S8 reports the same data present in Figure 13a after the normalization for $b_{abs(\lambda)}$ and for the corresponding CS HR_{BC} and HR_{BrC} values. Results first show that the relative decrease of the HR_{BrC}, from 0 to 8 oktas, was 12±6% lower compared to that of HR_{BC}, or, in other words, it was the decrease the HR_{BC} that was 12±6% higher compared to that of HR_{BrC} A counter-intuitive consequence of this analysis is that, compared to CS, cloudy conditions suppress much more the HR_{BC} with respect to HR_{BrC}. The diffuse component of the HR

560   was the only one that kept an opposite behavior after the normalization for $b_{abs(\lambda)}$. The decrease of $HR_{BrC,dif}$ was 21±6% higher compared to that of $HR_{BC,dif}$ (from clear sky situation to overcast ones); however this value is lower than the 38±6% reported in section 3.4.1 before the normalization for $b_{abs(\lambda)}$ meaning that, even at equal absorption, the diffuse component of radiation plays a role in affecting the BrC response. This means that cloudiness and clouds not only affect absolute values of both HR_{BC} and HR_{BrC} but they markedly affect their ratio.

565   This pattern can be related to the different APE (section 2.3.3) that the direct and diffuse radiations feature in different sky conditions (Figure 14). Higher APE values describe the shift of a radiation spectrum towards UV-blue region and vice versa (section 2.3.3). Figure 14 shows that while APE_{dir} slightly increases towards overcast conditions, APE_{dif} strongly decreases going from clear sky to 8 oktas. The $APE_{dif,dir}$ behavior can easily be explained considering the features of the direct and diffuse radiation spectra (Figure S9). In fact, in clear sky

570   conditions, the diffuse radiation is characterized by a high density in the UV-blue high energy region with respect to the direct radiation, which indeed is depleted in that region by the molecular Rayleigh scattering. APE_{dir} in clear sky conditions is in fact 1.89±0.01 eV, lower than the 2.20±0.01 eV of APE_{dif} (Figure 14). Conversely, in cloudy conditions (Figure 14 and Figure S9) $F_{dif,\lambda}$ and $F_{dir,\lambda}$ behave similarly and the APE_{dif} values equals that of APE_{dir}: 1.99±0.01 eV. The BrC has the capacity to absorb much more radiation in the UV-blue region (featuring higher

575   AAE of 3.49±0.01, compared to ~1 of BC). It follows that, depending on sky conditions, different parts of the absorption spectra are important for BrC relative to BC. In this respect, ΔAPE_{dir} (cloudy-CS) was $0.11\pm3*10^{-3}$ eV while ΔAPE_{dif} was 2 times higher ($0.22\pm2*10^{-3}$ eV). This explains the behavior of $HR_{BC,dir}$ and $HR_{BrC,dir}$ and of $HR_{BC,dif}$ and $HR_{BrC,dif}$ after the normalization for $b_{abs(\lambda)}$. However, they do not explain the behavior of the total HR_{BC} and HR_{BrC} with respect to cloudiness: the absolute amount of direct and diffuse radiation F_{dir}, F_{dif} (and not

580   only their spectral feature) has to be accounted for. Thus, the APE for the total sky radiation was determined as a weighted average with respect to the absolute amount of F_{dir} and F_{dif} in function of cloudiness expressed in oktas; results are reported in Figure 14 and clearly show an increasing APE_{tot} from clear sky to cloudy conditions, approaching APE_{dif} at okta=8. This APE_{tot} feature explain the counter-intuitive property that cloudy conditions suppress much more the HR_{BC} with respect to HR_{BrC}, as shown above.

585   We have shown that different cloud types are responsible for the different cloudiness (Section 3.3 and Figure 7b). It is worth to explore the relationship between cloud type and both HR_{BC} and HR_{BrC} as previously done for the total LAA HR (Figure 10). Also in this case, the variability of the HR induced by radiation was decoupled from

that due to $b_{abs(\lambda)}$ by normalizing HR_{BC} and HR_{BrC} for the adimensional integral of $b_{abs(\lambda)}$ over the whole aethalometer spectrum. We found a strong linear relationship between the mean cloudiness (in oktas) and the

590 percent decrease of both (BC and BrC) HRs with respect to those in clear sky conditions (Figure 15). These results were obtained by averaging the cloudiness (in oktas) for each cloud type (as detected in section 3.3) and combining them with percentage decrease of HR_{BC} and HR_{BrC} (again averaged for each cloud type) with respect to clear sky conditions. Overall, the derived linear regression indicates for both HR_{BC} and HR_{BrC} a decrease of about 12% per oktas (with high R^2). Knowledge of the dominant cloud types associated to the different cloud cover also allows

595 us to associate this decrease to specific cloud types. In particular, Ci were found to produce a modest impact on cloudiness (0.50±0.05 oktas) decreasing the HR_{BC} and HR_{BrC} by ~1-6%, respectively. Instead, Cu (1.76±0.09 oktas) decreased the HR_{BC} and HR_{BrC} by -31±12% and -26±7%, respectively. CiCu-CiSt were associated to an averaged oktas of 3.56±0.14, and were responsible for a -60±8% and -54±4% decrease of the HR_{BC} and HR_{BrC}. Their impact was comparable to that of AlCu (4.11±0.18 oktas): -60±6% and -46±4% decrease of the HR_{BC} and

600 HR_{BrC}. StCu (4.68±0.10 oktas) had a higher impact, decrasing HR_{BC} and HR_{BrC} of -63±6% and -58±4%. The highest impact was given by AlSt (6.57±0.15 oktas; -78±5% and -73±4% of HR_{BC} and HR_{BrC}) and finally by St (oktas: 7.19±0.04) that suppressed the HR_{BC} and HR_{BrC} by a factor of -85±5% and -83±3%, respectively. These results confirm that, on average, the HR_{BC} is more affected by cloudy conditions than HR_{BrC}, further proving that the presence of different cloud types in different proportions in the sky can bring to inaccurate HR_{BC} and

605 HR_{BrC} estimations if clear sky assumptions are improperly used to model the aerosol DRE. Particularly, if clear sky is assumed improperly, HR_{BC} and HR_{BrC} can be overestimated up to a factor of ~6 in highly cloudy St conditions. Thus, the aerosol DRE and related HR has to be properly calculated in the presence of clouds for correct future scenario of our climate system.

610 **Conclusions**

The heating rates (HR) associated to Black Carbon (BC) and Brown Carbon (BrC) (HR_{BC} and HR_{BrC}) were experimentally determined at high time resolution (5-minutes) in the Po Valley and further examined in relation to sky conditions to determine the impact of cloud-aerosol-radiation interactions on the atmospheric heating. Results showed a constant decrease of HR with increasing cloudiness of the atmosphere. From the obtained results,

615 the error (in %) associated to HR radiative transfer calculations in case of a simplified but incorrect assumption of clear sky was calculated as a function of the real (observed) cloudiness showing overestimations up to 470%. The effect of different cloud types on the HR was also investigated. While cirrus were characterized by a modest impact cumulus, cirrocumulus-cirrostratus and Altocumulus: suppressed the HR of both BC and BrC by a factor of ~2. Stratocumulus, altostratus stratus suppressed the HR_{BC} and HR_{BrC} up to 80%. The cloudiness also changed the

620 diurnal pattern of HR with possible feedbacks on planetary boundary layer dynamics and/or regional circulation systems. Thus, any inappropriate use of clear sky assumption in models will also reflect on the modelled HR-triggered feedbacks.

Finally, the cloud impact on the solar radiation spectrum affected more, on average, the HR_{BC} than HR_{BrC}. This means that cloudiness and clouds type not only affect absolute values of both HR_{BC} and HR_{BrC} but they markedly

625 affect their ratio further proving that the presence of different cloud types in different proportions in the sky can bring to inaccurate HR_{BC} and HR_{BrC} estimations if clear sky assumptions are improperly used.

Acknowledgements

This paper is an output of the GEMMA center in the framework of the MIUR project "Dipartimenti di Eccellenza
630   2018-2022". The authors want to acknowledge the COST action COLOSSAL CA16109, Aerosol d.o.o and LSI-
Lastem for the cooperation during the campaign.

Data Availability

Data will be available upon request.

635

Author contribution

Conceptualization, L. Ferrero, E. Bolzacchini, Grisa Mocnik, Martin Rigler and A. Gregoric; Methodology, L.
Ferrero, A. Gregoric, S. Cogliati, N. Losi, F. Barnaba, L. Di Liberto, G.P. Gobbi; Data Investigation, L. Ferrero,
A. Gregoric, S. Cogliati, F. Barnaba, G. Mocnik, M. Rigler; Resources, E. Bolzacchini, M. Rigler; Original Draft
640   Preparation, L. Ferrero; Writing-Review & Editing, L. Ferrero, A. Gregoric, G. Mocnik and F. Barnaba;
Supervision, G. Mocnik, Martin Rigler, F. Barnaba, E. Bolzacchini.

Conflict of interest

The authors declare no conflict of interest. The funders had no role in the design of the study; in the collection,
645   analyses, or interpretation of data; in the writing of the manuscript, and in the decision to publish the results.

References

Andreae, M., Ramanathan, V.: Climate's Dark Forcings. Science, 340 (2002), 280–281, 2013.

Bikkina, S., Sarin, M.M.: Light absorbing organic aerosols (brown carbon) over the tropical Indian Ocean: impact
650   of biomass burning emissions. Environ. Res. Lett., 8 (4), 044042, 2013.

Barnaba, F. and Gobbi, G. P.: Aerosol seasonal variability over the Mediterranean region and relative impact of
maritime, continental and Saharan dust particles over the basin from MODIS data in the year 2001, Atmospheric
Chemistry and Physics, 4(9/10), 2367–2391, doi:10.5194/acp-4-2367-2004, 2004.

Barnaba, F., Putaud, J.P., Gruening, C., Dell'Acqua, A., Dos Santos, S., 2010. Annual cycle in co-located in situ,
655   total-column, and height- resolved aerosol observations in the Po Valley (Italy): Implications for ground-level
particulate matter mass concentration estimation from remote sensing. J. Geophys. Res., 115, D19209,
doi:10.1029/2009JD013002.

Boers, R., de Haij, M. J., Wauben, W., Baltink, H. K., van Ulft, L. H., Savenije, M., & Long, C. N.: Optimized
fractional cloudiness determination from five ground-based remote sensing techniques. Journal of Geophysical
660   Research, 115, D24116. https://doi.org/10.1029/ 2010JD014661, 2010.

Bond, T. C., Doherty, S. J., Fahey, D. W., Forster, P. M., Berntsen, T., Deangelo, B. J., Flanner, M. G., Ghan, S.,
Kärcher, B., Koch, D., Kinne, S., Kondo, Y. and Quinn, P. K.: Bounding the role of black carbon in the climate
system : A scientific assessment, J. Geophys. Res., 118, 1–173, doi:10.1002/jgrd.50171, 2013.

Bond, T. C. and Bergstrom, R. W.: Light Absorption by Carbonaceous Particles: An Investigative Review, Aerosol
665   Sci. Tech., 40, 27–67, doi:10.1080/02786820500421521, 2006.

Calbó, J., Pagès, D., and González, J.-A.: Empirical studies of cloud effects on UV radiation: A review, Reviews of Geophysics, 43, n/a-n/a, 10.1029/2004RG000155, 2005.

Carbone, C., Decesari, S., Mircea, M., Giulianelli, L., Finessi, E., Rinaldi, M., Fuzzi, S., Marinoni, A., Duchi, R., Perrino, C., Sargolini, T., Vardè, M., Sprovieri, F., Gobbi, G. P., An- gelini, F., and Facchini, M. C.: Size-resolved aerosol chemical composition over the Italian Peninsula during typical summer and winter conditions, Atmos. Environ., 44, 5269–5278, doi:10.1016/j.atmosenv.2010.08.008, 2010.

Campbell, J.R., Lolli, S., Lewis, J.R., Gu, Y., and Welton, E. J.: Daytime Cirrus Cloud Top-of-the-Atmosphere Radiative Forcing Properties at a Midlatitude Site and Their Global Consequences. J. Appl. Meteorol. Climatol., 55, 1667–1679, 2016.

Chung, C. E., Ramanathan, V., Decremer, D. Observationally constrained estimates of carbonaceous aerosol radiative forcing. Proceedings of the National Academy of Sciences of the United States of America, 109 (29), 11624–11629, 2012.

Collaud Coen M., Weingartner E., Apituley A., Ceburnis D., Fierz-Schmidhauser R., Flentje H., Henzing J.S., Jennings S.G., Moerman M., Petzold A., Schmid O., and Baltensperger U. Minimizing light absorption measurement artifacts of the Aethalometer: evaluation of five correction algorithms. Atmos. Meas. Tech., 3, 457–474, 2010.

Costabile, F., Barnaba, F., Angelini, F. and Gobbi, G. P.: Identification of key aerosol populations through their size and composition resolved spectral scattering and absorption, Atmospheric Chemistry and Physics, 13(5), 2455–2470, doi:10.5194/acp-13-2455-2013, 2013.

Croke, M. S., Cess, R. D. and Hameed, S.: Regional cloud cover change associated with global climate change: Case studies for three regions of the United States, Journal of Climate, 12(7), 2128–2134, 1999.

Diémoz, H., Barnaba, F., Magri, T., Pession, G., Dionisi, D., Pittavino, S., Tombolato, I.K.F., Campanelli, M., Della Ceca, L., Hervo, M., Di Liberto, L., Ferrero, L., Gobbi, G.P.: Transport of Po Valley aerosol pollution to the northwestern Alps. Part 1: phenomenology, Atmos. Chem. Phys., 19, 3065–3095, https://doi.org/10.5194/acp-19-3065-2019, 2019a.

Diémoz, H., Gobbi, G.P., Magri, T., Pession, G., Pittavino, S., Tombolato, I.K.F., Campanelli, M., Barnaba, F.: Transport of Po Valley aerosol pollution to the northwestern Alps. Part 2: Long-term impact on ari quality, Atmos. Chem. Phys., 19, 10129–10160, 2019 https://doi.org/10.5194/acp-19-10129-2019 2019b.

Dionisi, D., Barnaba, F., Diémoz, H., Di Liberto, L. and Gobbi, G. P.: A multiwavelength numerical model in support of quantitative retrievals of aerosol properties from automated lidar ceilometers and test applications for AOT and PM10 estimation, Atmospheric Measurement Techniques, 11(11), 6013–6042, doi:10.5194/amt-11-6013-2018, 2018.

IPCC, 2013: Climate Change 2013: The Physical Science Basis. Cambridge University Press, Cambridge, United Kingdom and New York, USA, 2013.

Duchon, C.E., O'Malley, M.: Estimating Cloud Type from Pyranometer Observations. J. App. Meteorology, 38, 132–141, 1999.

Eleftheriadis, K., Vratolis, S. and Nyeki, S.: Aerosol black carbon in the European Arctic: Measurements at Zeppelin station, Ny-Ålesund, Svalbard from 1998-2007, Geophysical Research Letters, 36(2), doi:10.1029/2008GL035741, 2009.

Ehnberg, J. S. G. and Bollen, M. H. J.: Simulation of global solar radiation based on cloud observations, Solar

Energy, 78(2), 157–162, doi:10.1016/j.solener.2004.08.016, 2005.

Feister, U., Cabrol, N., and Häder, D.: UV Irradiance Enhancements by Scattering of Solar Radiation from Clouds, Atmosphere, 6, 1211-1228, 10.3390/atmos6081211, 2015.

Ferrero, L., Riccio, A., Perrone, M. G., Sangiorgi, G., Ferrini, B. S., and Bolzacchini, E.: Mixing height
710   determination by teth- ered balloon-based particle soundings and modeling simulations, Atmos. Res, 102, 145–156, doi:10.1016/j.atmosres.2011.06.016, 2011a.

Ferrero, L., Mocnik, G., Ferrini, B. S., Perrone, M. G., Sangiorgi, G. and Bolzacchini, E.: Vertical profiles of aerosol absorption coefficient from micro-Aethalometer data and Mie calculation over Milan., Sci. Total Environ., 409(14), 2824–37, doi:10.1016/j.scitotenv.2011.04.022, 2011b.

715   Ferrero, L., Cappelletti, D., Moroni, B., Sangiorgi, G., Perrone, M. G., Crocchianti, S. and Bolzacchini, E.: Wintertime aerosol dynamics and chemical composition across the mixing layer over basin valleys, Atmos. Environ., 56, 143–153, doi:10.1016/j.atmosenv.2012.03.071, 2012.

Ferrero, L., Castelli, M., Ferrini, B.S., Moscatelli, M., Perrone, M.G., Sangiorgi, G., Rovelli, G., D'Angelo, L., Moroni, B., Scardazza, F., Mocnik, G., Bolzacchini, E., Petitta, M., Cappelletti, D.: Impact of Black Carbon
720   Aerosol over Italian basin valleys: high resolution measurements along vertical profiles, radiative forcing and heating rate. Atmos. Chem. Phys., 14, 9641–9664, 2014.

Ferrero, L., Cappelletti, D., Busetto, M., Mazzola, M., Lupi, A., Lanconelli, C., Becagli, S., Traversi, R., Caiazzo, L., Giardi, F., Moroni, B., Crocchianti, S., Fierz, M., Mocnik, G., Sangiorgi, G., Perrone, M.G., Maturilli, M., Vitale, V., Udisti, R., Bolzacchini, E.: Vertical profiles of aerosol and black carbon in the Arctic: a seasonal
725   phenomenology along 2 years (2011–2012) of field campaigns, Atmos. Chem. Phys., 16(19), 12601–12629, https://doi.org/10.5194/acp-16-12601-2016, 2016.

Ferrero L., Močnik G., Cogliati S., Gregorič A., Colombo R., Bolzacchini E.: Heating Rate of Light Absorbing Aerosols: Time-Resolved Measurements, the Role of Clouds, and Source Identification. Environ. Sci. Tech., 52, 3546−3555, DOI: 10.1021/acs.est.7b04320, 2018.

730   Ferrero, L., Sangiorgi, G., Perrone, M.G., Rizzi, C., Cataldi, M., Markuszewski, P., Pakszys, P., Makuch, P., Petelski, T., Becagli, S., Traversi, R., Bolzacchini, E., Zielinski, T.: Chemical Composition of Aerosol over the Arctic Ocean from Summer ARctic EXpedition (AREX) 2011 – 2012 Cruises: Ions, Amines, Elemental Carbon, Organic Matter, Polycyclic Aromatic Hydrocarbons, n-Alkanes, Metals, and Rare Earth Elements. Atmosphere 10, 54, 1-32, doi:10.3390/atmos10020054, 2019°.

735   Ferrero, L., Ritter, C., Cappelletti, D., Moroni, B., Močnik, G., Mazzola, M., Lupi, A., Becagli, S., Traversi, R., Cataldi, M., Neuber, R., Vitale, V., Bolzacchini, E: Aerosol optical properties in the Arctic: the role of aerosol chemistry and dust composition in a closure experiment between Lidar and tethered balloon vertical profiles. Sci. Tot. Environ., 686, 452–467, doi.org/10.1016/j.scitotenv.2019.05.399, 2019b.

Duchon, C. E. and O'Malley, M. S.: Estimating cloud type from pyranometer observations, Journal of Applied
740   Meteorology, 38(1), 132–141, doi:10.1175/1520-0450, 1999.

Jacobson, M. Z. Control of fossil-fuel particulate black carbon and organic matter, possibly the most effective method of slowing global warming. J. Geophys. Res., 107 (D19), 4410, 2002.

Jacobson, M.Z.: Short-term effects of controlling fossil-fuel soot, biofuel soot and gases, and methane on climate, arctic ice, and air pollution health, J. Geophys. Res., 115, D14209, doi:10.1029/2009JD013795, 2010.

745   Junker, C., Jennings, S. G., and Cachier, H. Aerosol light absorption in the North Atlantic: trends and seasonal characteristics during the period 1989 to 2003. Atmos. Chem. Phys., 6, 1913– 1925, 2006.

Kaufman, Y.J., Tanré, D., Boucher, O.: A satellite view of aerosols in the climate system. Nature 419, 215–223, 2002.

Koch, D., Schulz, M., Kinne, S., McNaughton, C., Spackman, J. R., Balkanski, Y., Bauer, S., Berntsen, T., Bond, 750   T. C., Boucher, O., Chin, M., Clarke, A., De Luca, N., Dentener, F., Diehl, T., Dubovik, O., Easter, R., Fahey, D. W., Feichter, J., Fillmore, D., Freitag, S., Ghan, S., Ginoux, P., Gong, S., Horowitz, L., Iversen, T., Kirkevåg, A., Klimont, Z., Kondo, Y., Krol, M., Liu, X., Miller, R., Montanaro, V., Moteki, N., Myhre, G., Penner, J. E., Perlwitz, J., Pitari, G., Reddy, S., Sahu, L., Sakamoto, H., Schuster, G., Schwarz, J. P., Seland, Ø., Stier, P., Takegawa, N., Takemura, T., Textor, C., van Aardenne, J. A., Zhao, Y.: Evaluation of black carbon estimations 755   in global aerosol models. Atmos. Chem. Phys., 9, 9001–9026, 2009, doi:10.5194/acp-9-9001-2009.

Koch, D., Del Genio, A.D.: Black carbon semi-direct effects on cloud cover: review and synthesis. Atmos. Chem. Phys. 10, 7685–7696, 2010, doi:10.5194/acp-10-7685-2010.

Koren, I., Kaufman, Y.J., Remer, L.A., Martins, J.V.: Measurments of the effect of amazon smoke on inhibition of cloud formation. Science, 303, 1342-1345, 2004.

760   Koren, I., Martins, J.V., Remer, L.A., Afargan, H.: Smoke invigoration versus inhibition of clouds over the amazon, Science, 321, 946-949, 2008.

Kumar, N. K., Corbin, J. C., Bruns, E. A., Massabó, D., Slowik, J. G., Drinovec, L., Močnik, G., Prati, P., Vlachou, A., Baltensperger, U., Gysel, M., El-Haddad, I., and Prévôt, A. S. H.: Production of particulate brown carbon during atmospheric aging of residential wood-burning emissions, Atmos. Chem. Phys., 18, 17843–17861, 765   https://doi.org/10.5194/acp-18-17843-2018, 2018.

Lolli, S., Madonna, F., Rosoldi, M., Campbell, J.R., Welton, E.J., Lewis, J.R., Gu, Y., Pappalardo G.: Impact of varying lidar measurement and data processing techniques in evaluating cirrus cloud and aerosol direct radiative effects. Atmos. Meas. Tech., 11, 1639–1651, 2018, https://doi.org/10.5194/amt-11-1639-2018.

López, M. L., Palancar, G. G., and Toselli, B. M.: Effect of different types of clouds on surface UV-B and total 770   solar irradiance at southern mid-latitudes: CMF determinations at Córdoba, Argentina, Atmos. Environ., 43, 3130-3136, http://dx.doi.org/10.1016/j.atmosenv.2009.02.065, 2009.

Martucci, G., Milroy, C., & O'Dowd, C. D.: Detection of cloud-base height using Jenoptik CHM15K and Vaisala CL31 ceilometers. Journal of Atmospheric and Oceanic Technology, 27, 305–318. https://doi.org/10.1175/2009JTECHA1326.1, 2010.

775   Myhre, G., Samset, B. H., Schulz, M., Balkanski, Y., Bauer, S., Berntsen, T. K., Bian, H., Bellouin, N., Chin, M., Diehl, T., Easter, R. C., Feichter, J., Ghan, S. J., Hauglustaine, D., Iversen, T., Kinne, S., Kirkeväg, A., Lamarque, J. F., Lin, G., Liu, X., Lund, M. T., Luo, G., Ma, X., Van Noije, T., Penner, J. E., Rasch, P. J., Ruiz, A., Seland, Skeie, R. B., Stier, P., Takemura, T., Tsigaridis, K., Wang, P., Wang, Z., Xu, L., Yu, H., Yu, F., Yoon, J. H., Zhang, K., Zhang, H. and Zhou, C.: Radiative forcing of the direct aerosol effect from AeroCom Phase II 780   simulations, Atmospheric Chemistry and Physics, 13(4), 1853–1877, doi:10.5194/acp-13-1853-2013, 2013.

Massabò, D., Caponi, L., Bernardoni, V., Bove, M.C., Brotto, P., Calzolai,, G., Cassola, F., Chiari, M., Fedi, M.E., Fermo, P., Giannoni, M., Lucarelli, F., Nava, S., Piazzalunga, A., Valli, G., Vecchi, R., Prati, P.: Multi-wavelength optical determination of black and brown carbon in atmospheric aerosols, Atmos. Environ., 108, 1-12, 2015.

Maugeri, M., Bagnati, Z., Brunetti, M. and Nanni, T.: Trends in Italian total cloud amount, 1951-1996, Geophysical Research Letters, 28(24), 4551–4554, doi:10.1029/2001GL013754, 2001.

Moroni, B., Cappelletti, D., Marmottini, F., Scardazza, F., Ferrero, L., and Bolzacchini, E.: Integrated single particle-bulk chemical approach for the characterization of local and long range sources of particulate pollutants, Atmos. Environ., 50, 267–277, doi:10.1016/j.atmosenv.2011.12.022, 2012.

Moroni, B., Ferrero, L., Crocchianti, S., Perrone, M. G., Sangiorgi, G., Bolzacchini, E., and Cappelletti, D.: Aerosol dynamics upon Terni basin (Central Italy): results of integrated vertical profile measurements and electron microscopy analyses, Rend. Lincei, 24, 319–328, doi:10.1007/s12210-013-0230-8, 2013.

Mims, F. E., and Frederick, J. E.: Cumulus clouds and UV-B, Nature, 371, 291, 1994.

Myhre, G., Samset, B. H., Schulz, M., Balkanski, Y., Bauer, S., Berntsen, T. K., Bian, H., Bellouin, N., Chin, M., Diehl, T., Easter, R. C., Feichter, J., Ghan, S. J., Hauglustaine, D., Iversen, T., Kinne, S., Kirkevåg, A., Lamarque, J. F., Lin, G., Liu, X., Lund, M. T., Luo, G., Ma, X., Van Noije, T., Penner, J. E., Rasch, P. J., Ruiz, A., Seland, Skeie, R. B., Stier, P., Takemura, T., Tsigaridis, K., Wang, P., Wang, Z., Xu, L., Yu, H., Yu, F., Yoon, J. H., Zhang, K., Zhang, H. and Zhou, C.: Radiative forcing of the direct aerosol effect from AeroCom Phase II simulations. Atmos. Chem. Phys., 13(4), 1853–1877, doi:10.5194/acp-13-1853-2013, 2013.

Nielsen, L., Prahm, L., Berkowicz, R., Conradsen, K.: Net incoming radiation estimated from hourly global radiation and/or cloud observations. J. Climatol., 1 ,255– 272, 1981.

Nordmann, S., Cheng, Y. F., Carmichael, G. R., M. Yu, M., Denier van der Gon, H. A. C., Zhang, Q., Saide, P. E., Pöschl, U., Su, H., Birmili, W., Wiedensohler, A. Atmospheric black carbon and warming effects influenced by the source and absorption enhancement in central Europe. *Atmos. Chem. Phys.* **2014**, *14*, 12683–12699, doi:10.5194/acp-14-12683-2014.

Perlwitz, J. and Miller, R. L.: Cloud cover increase with increasing aerosol absorptivity: A counterexample to the conventional semidirect aerosol effect, Journal of Geophysical Research Atmospheres, 115(8), 1–23, doi:10.1029/2009JD012637, 2010.

Petzold, A., Schloesser, H., Sheridan, P.J., Arnott, W.P., Ogren, J.A., Virkkula, A.: Evaluation of Multiangle Absorption Photometry for Measuring Aerosol Light Absorption. Aerosol Science and Technology, 39, 40–51, 2005.

Ramana, M. V, Ramanathan, V., Kim, D., Roberts, G. C. and Corrigan, C. E.: Albedo , atmospheric solar absorption and heating rate measurements with stacked UAVs, , 1931, 1913–1931, doi:10.1002/qj, 2007.

Ramanathan, V., Carmichael, G.: Global and regional climate changes due to black carbon. Nat. Geosci., 1, 221–227, 2008.

Ramanathan, V. and Feng, Y.: Air pollution, greenhouse gases and climate change: Global and regional perspectives, Atmos. Environ., 43(1), 37–50, doi:10.1016/j.atmosenv.2008.09.063, 2009.

Rodríguez, S., Van Dingenen, R., Putaud, J.-P., Dell'Acqua, A., Pey, J., Querol, X., Alastuey, A., Chenery, S., Ho, K.-F., Harrison, R., Tardivo, R., Scarnato, B., and Gemelli, V.: A study on the relationship between mass concentrations, chemistry and number size distribution of urban fine aerosols in Milan, Barcelona and London, Atmos. Chem. Phys., 7, 2217–2232, doi:10.5194/acp-7- 2217-2007, 2007.

Sandradewi J., Prevot A.S.H., Szidat S., Perron N., Alfarra M.R., Lanz V.A., Weingartner E., and Baltensperger U.: Using Aerosol Light Absorption Measurements for the Quantitative Determination of Wood Burning and Traffic Emission Contributions to Particulate Matter. Environ. Sci. Technol., 42, 3316–3323, 2008a.

825   Sandradewi, J., Prevot, A.S.H., Weingartner, E., Schmidhauser, R., Gysel, M., Baltensperger, U. A study of wood burning and traffic aerosols in an Alpine valley using a multi-wavelength Aethalometer. Atmos. Environ, 42, 101–112, 2008b.

Schwarz, J. P., Spackman, J. R., Gao, R. S., Watts, L. A., Stier, P., Schulz, M., Davis, S. M., Wofsy, S. C., and Fahey, D. W.: Global-scale black carbon profiles observed in the remote atmosphere and compared to models, Geophys. Res. Lett., 37, L18812, doi:10.1029/2010GL044372, 2010.

830   Shamjad, P. M., Tripathi, S. N., Pathak, R., Hallquist, M., Arola, A., Bergin, M. H.: Contribution of Brown Carbon to Direct Radiative Forcing over the Indo-Gangetic Plain. Environ. Sci. Technol., 49 (17), 10474–10481, 2015.

Stjern, C.W., Kristjansson J.E., Hansen A.W.: Global dimming and global brightening – an analysis of surface radiation and cloud cover data in northern Europe. Int. J. Climatol., 29, 643–653, 2009.

Tosca, M.G., Campbell, J., Garay, M., Lolli, S., Seidel, F.C., Marquis, J., Kalashnikova, O.: Attributing accelerated 835   summertime warming in the southeast united states to recent reductions in aerosol burden: Indications from vertically-resolved observations. Remote Sens., 9, 674, https://doi.org/10.3390/rs9070674, 2017.

Virkkula, A.: Correction of the Calibration of the 3-wavelength Particle Soot Absorption Photometer (3PSAP). Aerosol Science and Technology, 44, 706–712, 2010.

Wang, Z., Huang, X., and Ding, A.: Dome effect of black carbon and its key influencing factors: a one-dimensional 840   modelling study, Atmos. Chem. Phys., 18, 2821-2834, 10.5194/acp-18-2821-2018, 2018.

Weingartner, E., Saathoff, H., Schnaiter, M., Streit, N., Bitnar, B., Baltensperger, U.: Absorption of light by soot particles: determination of the absorption coefficient by means of aethalometers. Journal of Aerosol Science, 34 (10), 1445–1463, 2003.

Wiegner, M. and Geiß, A.: Aerosol profiling with the Jenoptik ceilometer CHM15kx, Atmos. Meas. Tech., 5, 845   1953–1964, doi:10.5194/amt-5-1953-2012, 2012.

Wofsy, S. C., the HIPPO Science Team and Cooperating Modellers and Satellite Teams: HIAPER Pole-to-Pole Observations (HIPPO): fine grained, global-scale measurements of climatically important atmospheric gases and aerosols, Philos. T. R. Soc., 369, 2073–2086, 2011.

WMO/GAW Aerosol Measurement Procedures, Guidelines and Recommendations 2nd Edition, GAW Report 850   227, World Meteorological Organization, Geneva, 2016.

Yang, M., Howell, S.G., Zhuang, J., Huebert, B.J.: Attribution of aerosol light absorption to black carbon, brown carbon, and dust in China and interpretations of atmospheric measurements during EAST-AIRE. Atmos. Chem. Phys., 9, 2035-2050, 2009.

Zotter, P., Herich, H., Gysel, M., El-Haddad, I., Zhang, Y., Mocnik,G., Hüglin,C., Baltensperger,U., Szidat,S., 855   Prevôt,A.S.H.: Evaluation of the absorption Ångström exponents for traffic and wood burning in the Aethalometer-based source apportionment using radiocarbon measurements of ambient aerosol. Atmos. Chem. Phys., 17, 4229−4249, 2017.

Level	Cloud type	SD	R	N cloud layer
	Stratus (St)	<120	0.0-0.4	1
Low (<2 km)	Cumulus (Cu)	/	0.8-1.1	1
	Stratocumulus (StCu)	/	0.4-0.8	1
Middle (2-7 km)	Altostratus (AlSt)	<120	0.0-0.4	1
	Altocumulus (AlCu)	>120	0.4-0.8	1
	Cirrus (Ci)	/	0.8-1.1	1
High (>7 km)	Cirrocumulus-Cirrostratus (CiCu-CiSt)	/	0.0-0.8	1
	Clear Sky (CS)	/	/	0

Table 1. Final criteria adopted for cloud classification. SD represents the standard deviation of the measured global irradiance with respect to the theoretical behaviour in clear sky conditions; R represents the ratio between observed global irradiance (F_{glo}) and the irradiance (E) expected at the same at the top of the atmosphere; N is cloud layer number detected by the lidar.

Month	Metric	T	P	eBC*	b_{abs}*	ADRE	$ADRE_{dir}$	$ADRE_{dif}$	$ADRE_{ref}$	HR	HR_{dir}	HR_{dif}	HR_{ref}	F_{glo}	F_{dir}	F_{dif}	F_{ref}
		°C	hPa	ng m⁻³	Mm⁻¹	mW m⁻³	mW m⁻³	mW m⁻³	mW m⁻³	K day⁻¹	K day⁻¹	K day⁻¹	K day⁻¹	W m⁻²	W m⁻²	W m⁻²	W m⁻²
Nov-15	mean	12.8	1003.8	4288	21.2	18.42	10.17	5.62	2.64	1.30	0.72	0.40	0.19	200	131	69	51
	CI 95%	0.2	0.3	96	0.5	0.61	0.44	0.18	0.08	0.04	0.03	0.01	0.01	5	1	5	1
Dec-15	mean	8.4	1012.8	6289	31.1	20.70	9.29	8.64	2.77	1.43	0.64	0.59	0.19	141	66	75	34
	CI 95%	0.1	0.1	97	0.5	0.68	0.48	0.24	0.08	0.05	0.03	0.02	0.01	4	2	3	1
Jan-16	mean	7.2	997.4	4198	20.8	12.57	5.53	5.26	1.79	0.87	0.38	0.36	0.12	150	85	65	36
	CI 95%	0.2	0.4	106	0.5	0.55	0.36	0.23	0.07	0.04	0.02	0.02	0.01	5	2	5	1
Feb-16	mean	9.2	995.5	2851	14.1	8.62	3.50	3.81	1.31	0.61	0.25	0.27	0.09	191	104	87	46
	CI 95%	0.1	0.3	74	0.4	0.35	0.23	0.14	0.05	0.02	0.02	0.01	0.00	6	3	6	2
Mar-16	mean	12.6	996.2	1535	7.6	7.58	2.96	3.28	1.34	0.54	0.21	0.23	0.10	310	174	136	77
	CI 95%	0.1	0.2	36	0.2	0.22	0.14	0.08	0.04	0.02	0.01	0.01	0.00	7	3	7	2

Table 2. Montlhy averaged data and confidence interval at 95% of temperature (T), pressure (P), equivalent black carbon (eBC), absorption coefficient (b_{abs}), absorptive direct radiative effect (ADRE) together with the heating rate (HR) divided into their direct (dir), diffuse (dif) and reflected (ref) components and, finally, global (F_{glo}), direct (F_{dir}), diffuse (F_{dif}) and reflected (F_{ref}) irradiances. * denotes Aethalometer data referred to λ=880 nm.
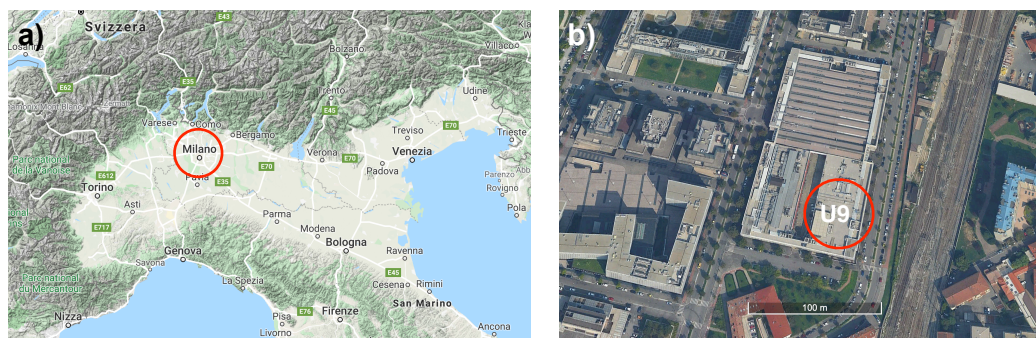
Figure 1. a) location of the Milano sampling site in the Po Valley, Italy; b) the U9 sampling site on the rooftop (10 m agl) of the University of Milano-Bicocca. The copyright holder of Figure 1 is GoogleMaps (©GoogleMaps).

CS (21 January 2016)

St (5 March 2016)

Ci (26 January 2016)

Cu (21 March 2016)
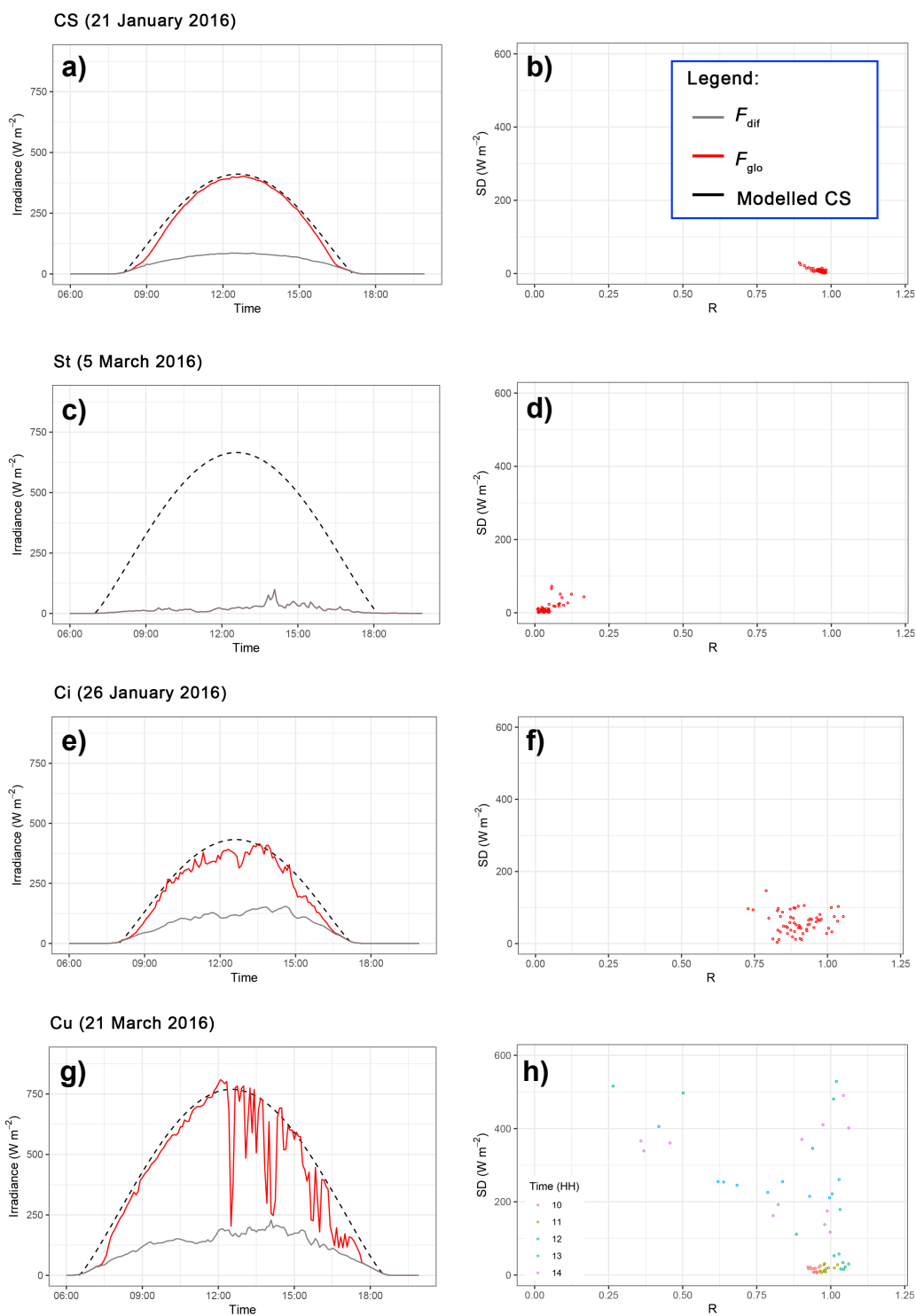
Figure 2. Cloud classification based on broadband solar radiation following Duchon & O'Malley (1999). Each row represents a different clout type in a specific day as a case study. The left columns represent the time series of global and diffuse measured solar irradiance and modelled clear sky irradiance (GHI), while the right column the scatter plot of the observed standard deviation of irradiance vs. the fraction of modelled clear sky irradiance. In the panel (h) different colors are related to different time (hours) of the day as reported in the legend.
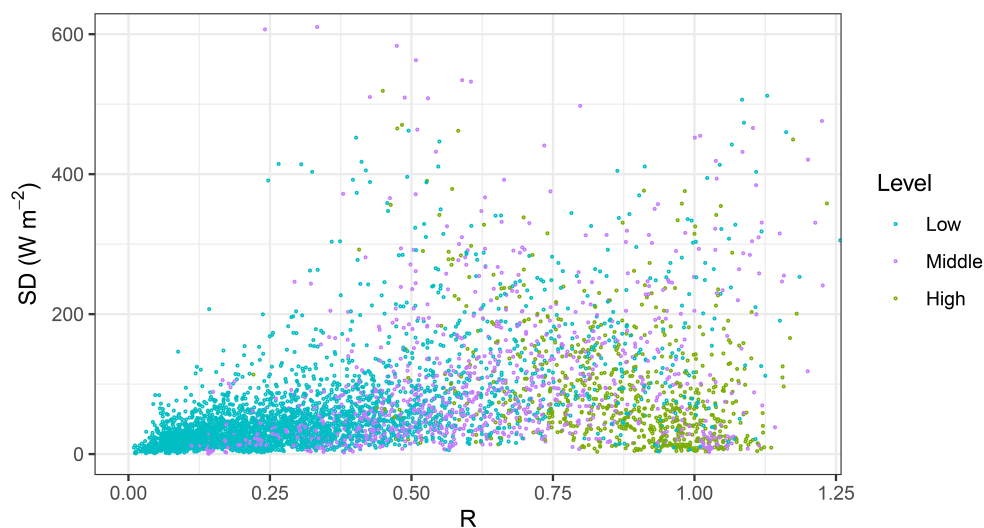
Figure 3. SD-R plot of the whole dataset concerning the cloud base altitude grouped into three levels, namely Low level clouds (<2 km), Middle altitude clouds (2-7 km) and High-altitude clouds (>7 km).
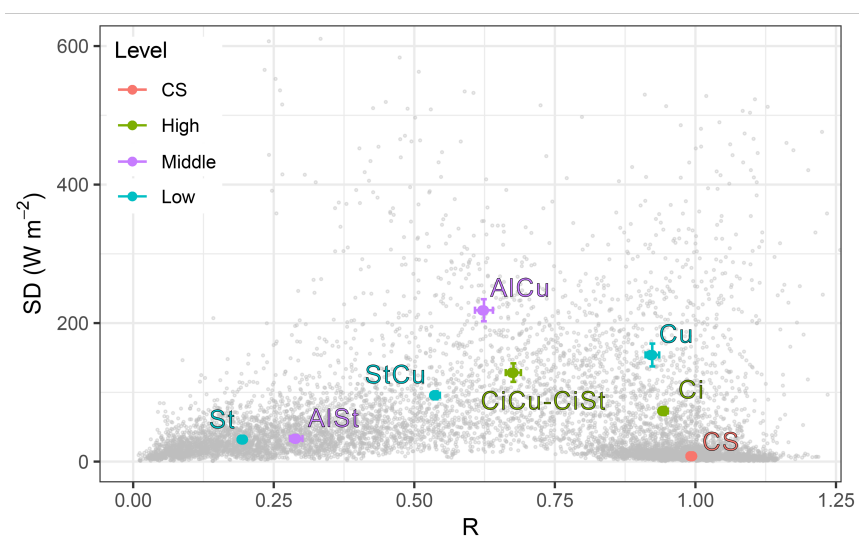
Figure 4. Cloud classification based on the improved broadband solar radiation following Duchon & O'Malley (1999) and Harrison et al. (2008) coupled with lidar data of cloud base height. From left to right: Stratus (St), Altostratus (AlSt), Stratocumulus (StCu), Altocumulus (AlCu), Cirruscumulus and Cirrusstratus (CiCu-CiSt), Cumulus (Cu), Cirrus

(Ci), and finally clear-sky (CS). The SD-R plot reports in grey the single data of the whole dataset, while centroids and 99% confidence bound of each cloud type are plotted in a color scale related to the cloud base level.
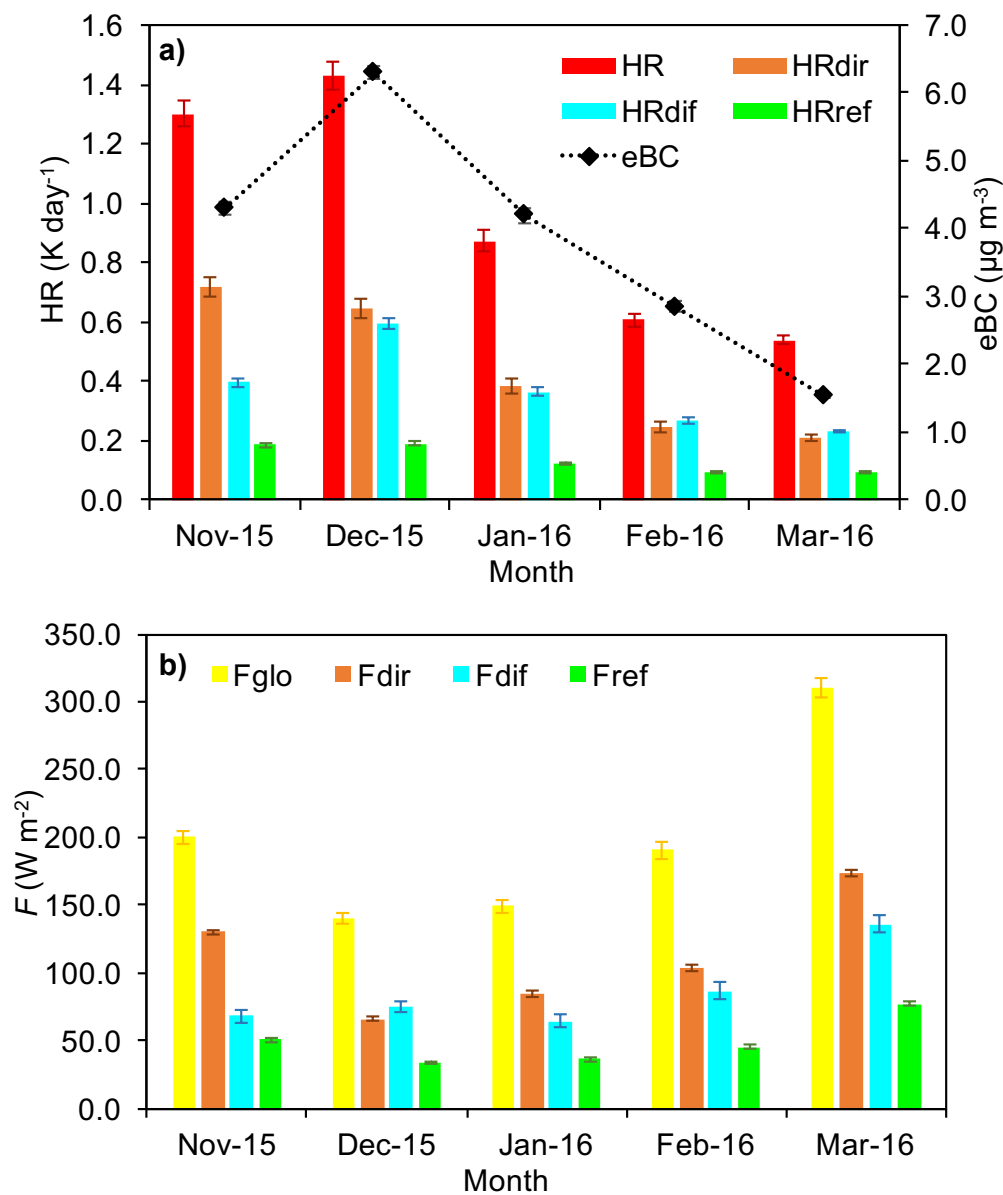
Figure 5. Monthly averaged values of: a) eBC, HR values and their direct, diffuse and reflected components (HR$_{dir}$, HR$_{dif}$ and HR$_{ref}$); b) global radiation values (F_{glo}) and their direct, diffuse and reflected components (F_{dir}, F_{dif} and F_{ref}).
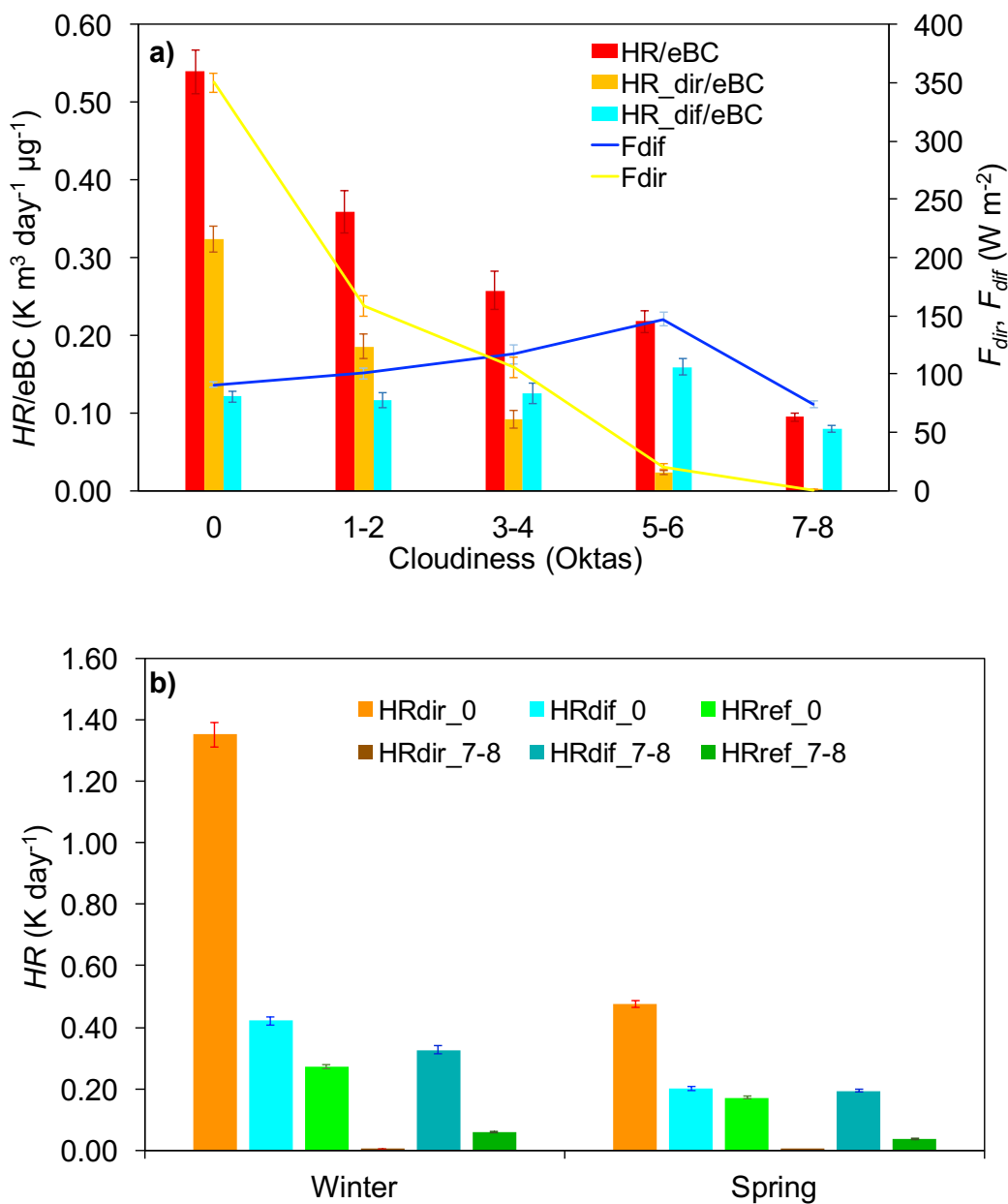
Figure 6. Monthly averaged values of: a) HR/eBC values together with their direct and diffuse components (HR$_{dir}$/eBC and HR$_{dif}$/eBC) and the direct and diffuse components of global radiation (F$_{dir}$ and F$_{dif}$); b) HR values and their direct, diffuse and reflected components (HR$_{dir}$, HR$_{dif}$ and HR$_{ref}$) during winter and spring both in clear sky (oktas=0) and cloudy (oktas=7-8) conditions.
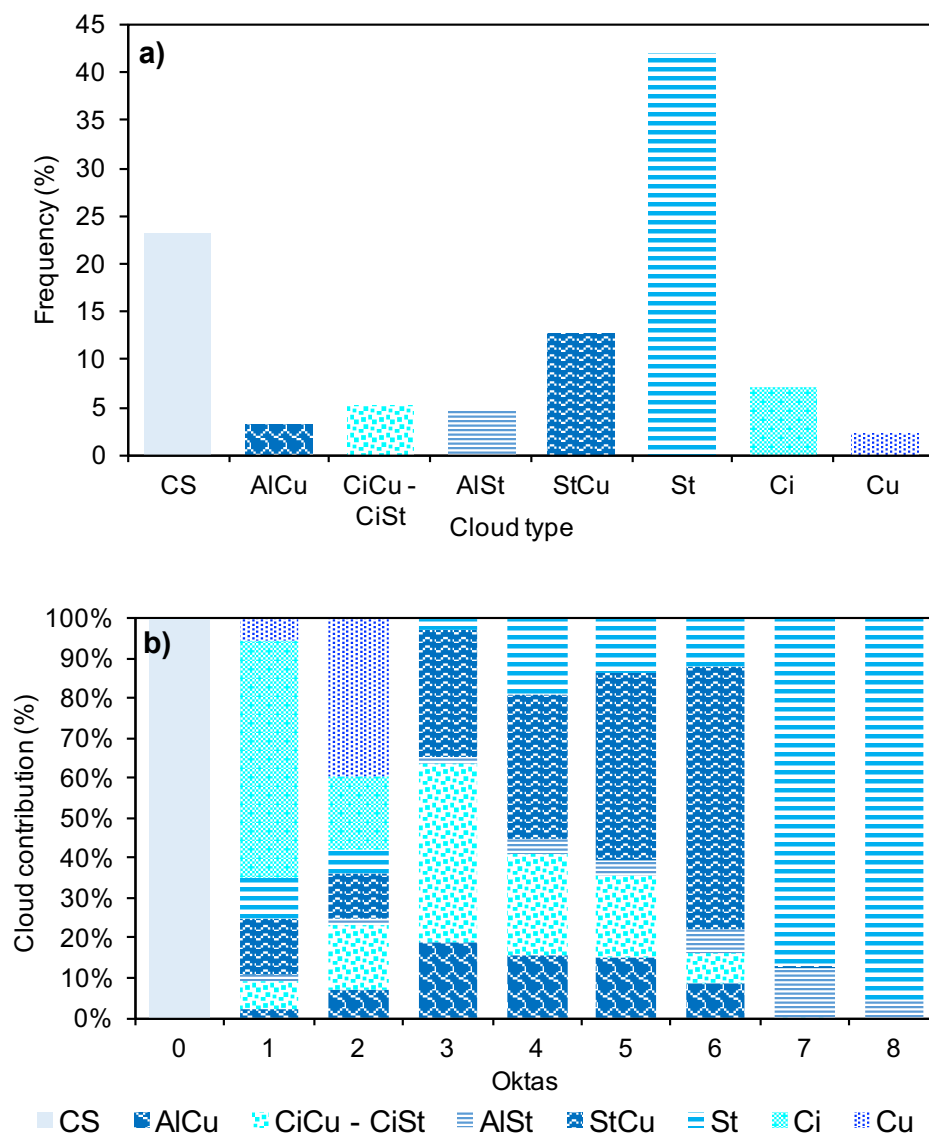
Figure 7. a) Time frequency (%) of the cloud type classified over the U9 site (CS means clear sky); b) contribution (%) of each cloud type to the oktas measured over the U9 site.
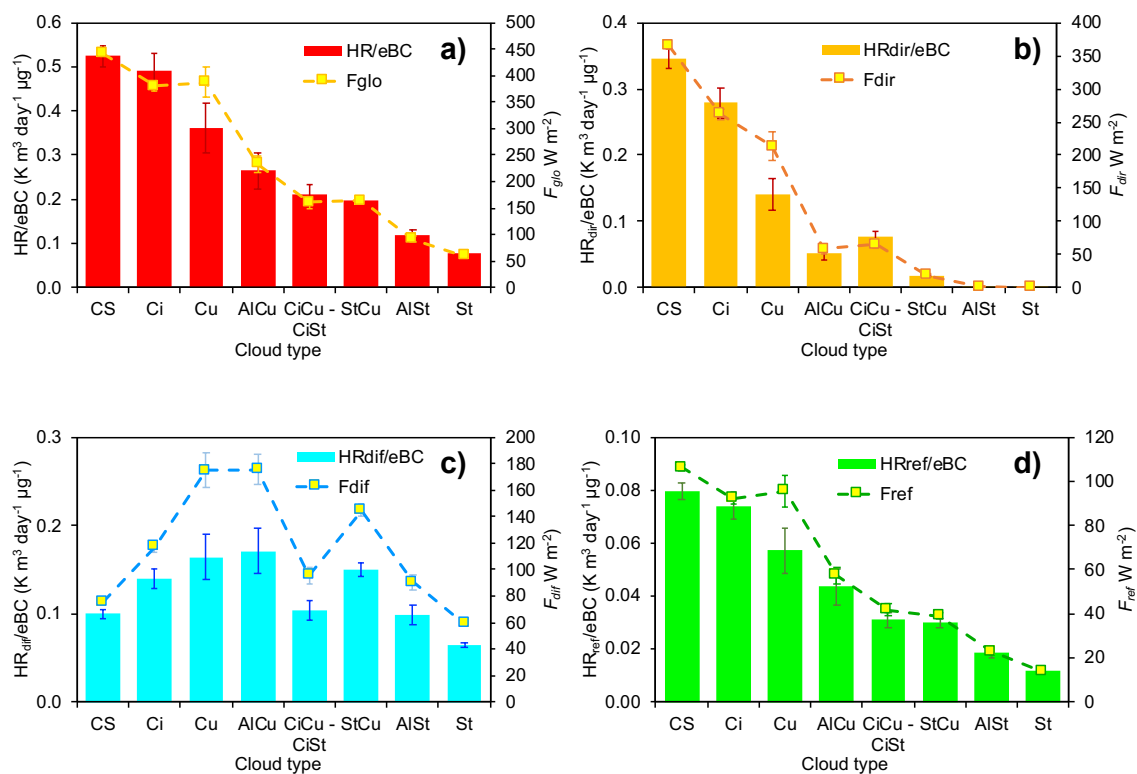
Figure 8. Impact of each cloud type on: HR/eBC and F_{glo} (a), HR$_{dir}$/eBC and F_{dir} (b), HR$_{dif}$/eBC and F_{dif} (c), HR$_{ref}$/eBC and F_{ref}.
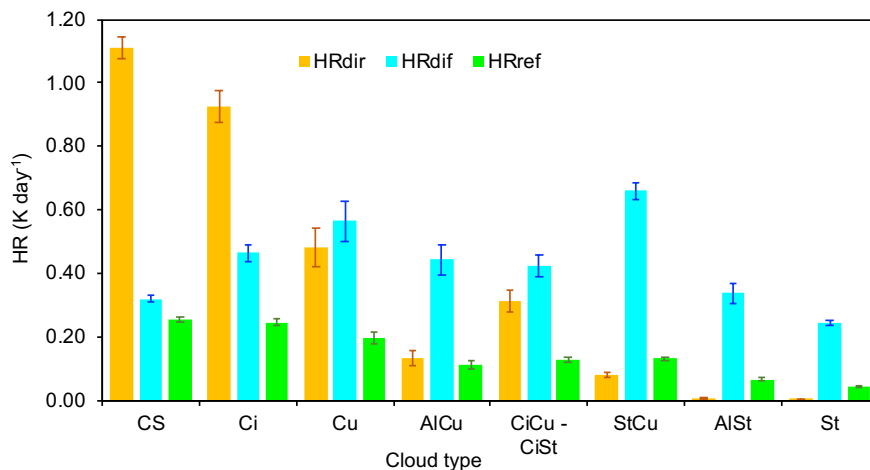
Figure 9. Average values of HR$_{dir}$, HR$_{dif}$ and HR$_{ref}$ in function of the cloud type.
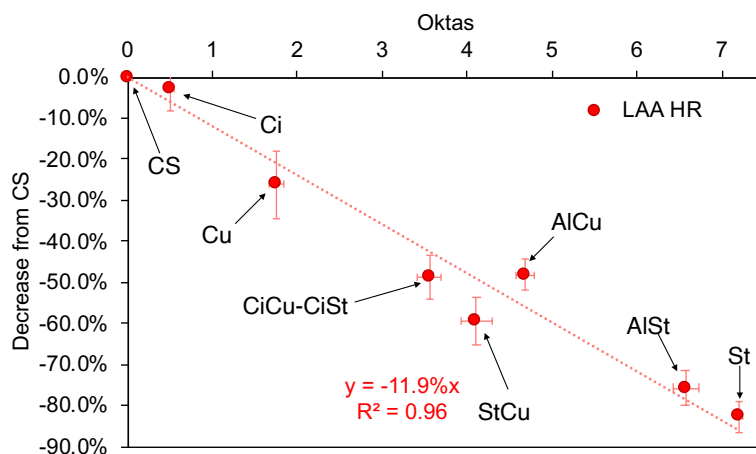
Figure 10. Percentage decrease of HR with respect to clear sky conditions in function of the oktas averaged for each cloud type.
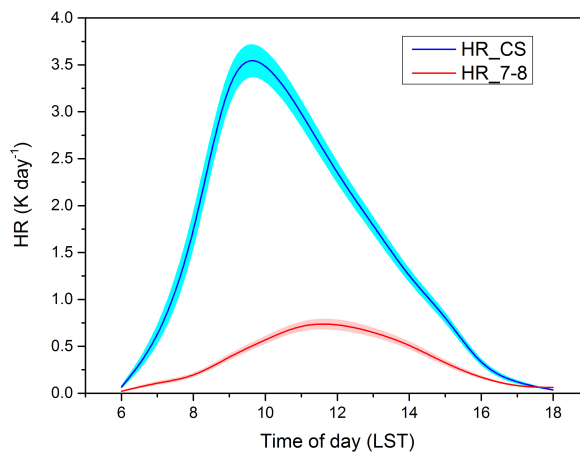
Figure 11. Diurnal pattern of the HR averaged for clear sky conditions and cloudy conditions (oktas=7-8).
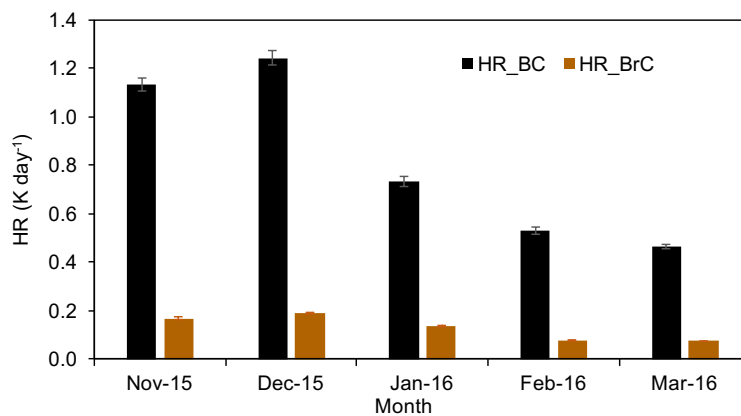
Figure 12. Monthly averaged data for the HR of both BC and BrC.
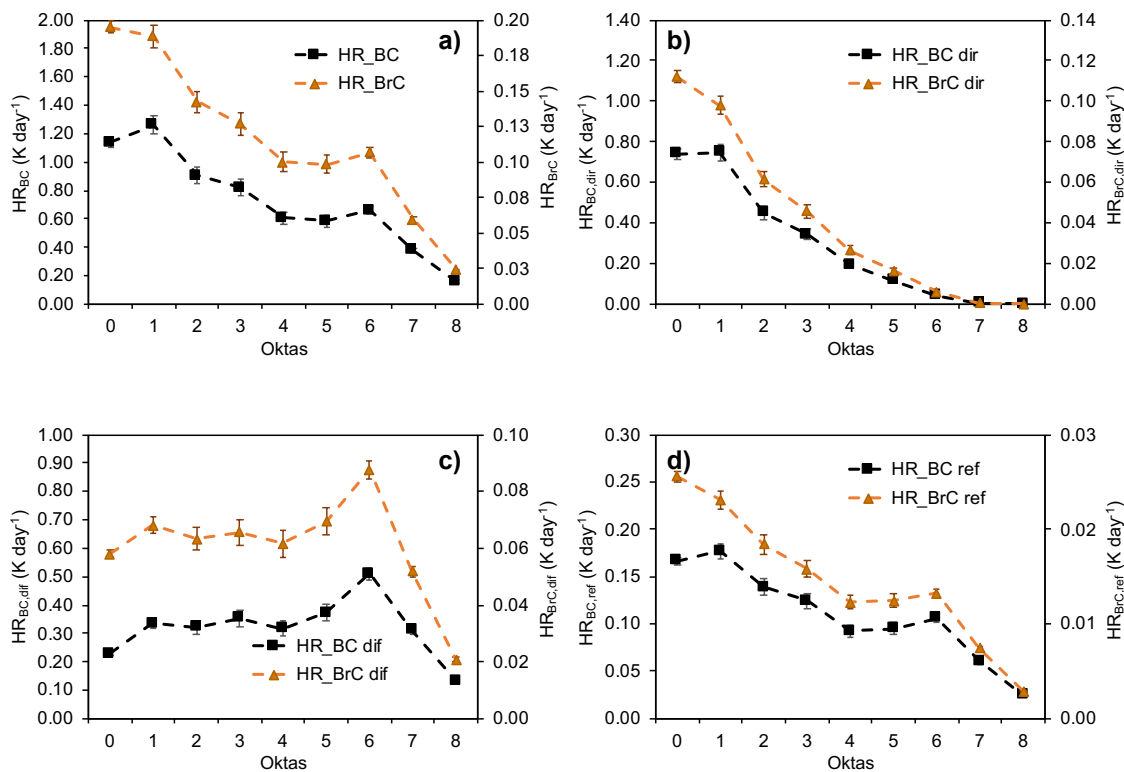
Figure 13. HR of BC and BrC in function of the oktas: a) total HR_{BC} and HR_{BrC}, b) direct component of both HR_{BC} and HR_{BrC} ($HR_{BC,dir}$ and $HR_{BrC,dir}$), c) diffuse component of both HR_{BC} and HR_{BrC} ($HR_{BC,dif}$ and $HR_{BrC,dif}$) and d) reflected component of both HR_{BC} and HR_{BrC} ($HR_{BC,ref}$ and $HR_{BrC,ref}$). Note that, due to the different magnitude of HR_{BC} and HR_{BrC}, the y-axis of HR_{BrC} in the four panels was chosen as 1/10 of that of HR_{BC}.
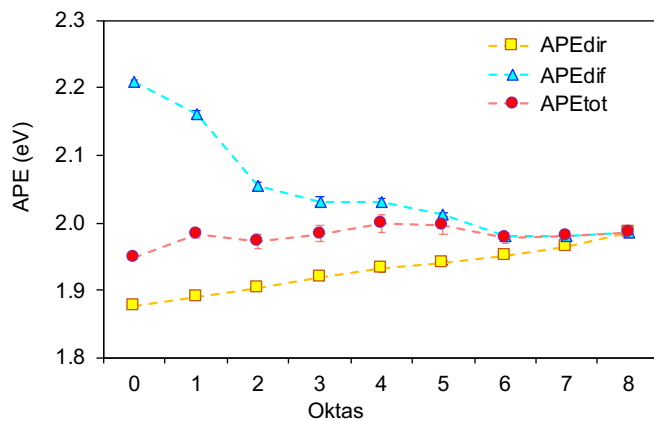
Figure 14. Direct and diffuse average photon energy of the radiation (APE_{dir} and APE_{dif}) together with the total impinging from sky (APE_{tot}).
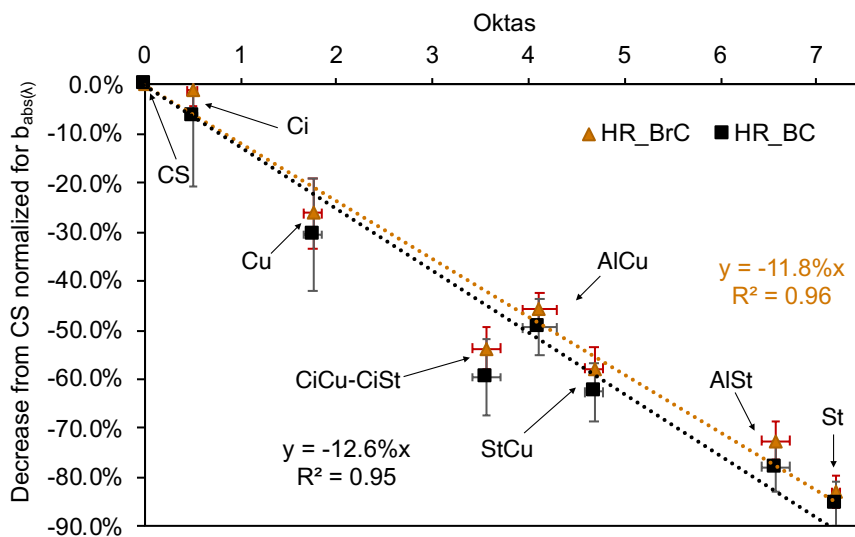
Figure 15. Percentage decrease of HR_{BC} and HR_{BrC} with respect to clear sky conditions in function of the oktas averaged for each cloud type.